Development of a quantum, magnetic-imaging platform for biophysical measurements

Isaac Shelby

A dissertation

submitted in partial fulfillment of the

requirements for the degree of

Doctor of Philosophy

University of Washington
2023

Reading Committee:
Paul Wiggins, Chair
Kai-Mei Fu
Miguel Morales

Program Authorized to Offer Degree:
Physics

University of Washington

Abstract

Development of a quantum, magnetic-imaging platform for biophysical measurements

Isaac Shelby

Chair of the Supervisory Committee:

Paul Wiggins
Departments of Physics, Bioengineering, and Microbiology

Single-molecule measurements help build up the fundamental understanding of many important biological functions. Due to the wide variety of molecules that have been studied, and the properties of these molecules that often make them difficult to directly image, many single-molecule experiments involve attaching a more-easily-observable object to the molecule in question. Whether that attached object is a fluorescent protein that a cell has been modified to attach to the desired target molecule or a immuno-functionalized sub-micron-scale bead, these probes can often only report on the position of the underlying molecule. This thesis presents the development of a sub-micron scale magnetic field imaging platform to allow for direct orientation measurements in single molecule, biological experiments. Following relevant background from the fields of single molecule experiment and quantum sensing, two experiments using this new imaging platform are presented. By combining the magnetic imaging platform with a novel quantum control system, video-rate magnetic imaging is possible. By combining the magnetic imaging platform with a magnetic tweezer system, a micro-magnetic torque balance is constructed, allowing for probing of single DNA strand bend stiffness. In both cases, statistical inference is applied to determine relevant magnetic particle parameters from magnetic field images to extract relevant information about the underlying system.

Acknowledgements

There are myriad people who help me along this journey in graduate school, both professionally and personally.

The MagPI team members during my tenure whose combined persistence and dedication to this project made any of it possible: Zeeshawn Kazi, Paul Wiggins, Kai-Mei Fu, Joey Turnbull, Ruhee Nirodi, Madeline Walters.

Wiggins Lab Members that I had the pleasure of sharing an office with over the years and whose help ranged from how to run basic microbiology protocols to how to best structure a talk to how to navigate graduate school: Sarah Mangiameli, Colin LaMont, Monica Cesinger, Julie Cass, Dean Huang, Kevin Cutler, James Choi, Teresa Lo, Dani Koch

The professors who have served on my advisory committee for their guidance in scientific approach and communication: Paul Wiggins, Kai-Mei Fu, Miguel Morales, Marcel den Nijs, Chip Asbury, Beth Traxler, and Steve Sharpe.

Beth Traxler again for allowing me to fumble around in her lab and whose help an advice were always available.

Catherine Provost and John Lombard for their advice and support during my time at UW.

Many more coworkers and professors in the department who have been part of my time in graduate school.

My friends and family who have offered support in all ways.

Thank you all.

Contents

1 Introduction **1**

1.1 Introduction 1

1.2 Challenges and Approaches 3

1.3 Outline 4

2 Motivation **5**

2.1 Introduction 5

2.2 Advantages of a single-molecule biological assay that is unbleachable and measures position and orientation. 5

2.3 Why DNA is a good candidate for orientation dependent measurements 6

3 Background **9**

3.1 Magnetic field sensing 9

3.1.1 Optically detected magnetic resonance in Nitrogen Vacancy Centers in Diamond . . 9

3.1.2 Going from magnetic field measurement to magnetic bead parameterization 13

3.2 Biological background on relevant DNA dynamics for the experiments presented. 14

3.2.1 Existing Models of DNA Mechanics and Experimental Approaches 14

3.2.2 DNA looping: biological relevance and model defying measurements 17

4 Wide-field dynamic magnetic microscopy using double-double quantum driving of a diamond defect ensemble **21**

4.1 Introduction 21

4.2 Experimental Methods . . . 23
4.3 Static Magnetic Imaging Modality . . . 25
4.3.1 Double Quantum Difference Imaging . . . 27
4.3.2 Double-Double Quantum Difference Imaging . . . 28
4.4 Wide-field Dynamic Magnetic Microscopy . . . 29

5 Development of single molecule DNA magnetic micro-torque balance 33
5.1 Introduction . . . 33
5.2 Magnetic micro-torque Balance Experimental Design . . . 33
5.3 Proof of Principle Measurement - Unconstrained Bead-DNA Attachment . . . 34
5.4 Nano-mechanical torque balance . . . 39
5.5 Probe orientation measured by quantum magnetic field imaging . . . 39
5.6 Dipole orientation illuminates distinct DNA binding configurations . . . 39
5.7 Bend stiffness measurement . . . 41
5.8 Conclusion and Outlook . . . 44

6 Inference in Image Analysis 47
6.1 From ODMR to magnetic fields . . . 47
6.1.1 From Magnetic fields to Dipole Parameters . . . 48
6.2 Least Squares from Maximum Likelihood Estimate . . . 49
6.3 Magnetic field gradient masking . . . 50

7 Outlook 55
7.1 Future Applications of DDQ . . . 55
7.2 Future Applications of micro-torsional DNA balance . . . 56

A Biological Protocols 73
A.1 PCR . . . 73
A.1.1 Relevant DNA sequences . . . 75
A.2 DNA cutting . . . 76

A.3 DNA tether construction 78
A.4 DNA cleanup 79

List of Figures

3.1 (a) Schematic of NV center. Circularly polarized light can be used to select for one possible transition, while linear polarized light allows for both. (b) Ground state of the NV center system for available z-spin projections. Zero field splitting and Zeeman shift denoted. Required polarization helicity indicated for transitions (c) Energy level diagram showing excited states for states in (b) as well as singlet states for non-radiative decay from $m = \pm 1$ excited states. Green arrows indicate the excitation to higher phononic sidebands. Red arrows indicate emission upon direct decay to ground state. There is an unlabeled emission transition from the excited to ground state for $m = \pm 1$ as well. Figure originally from [1] . . 10

3.2 **Panel A: An effective model for DNA mechanics.** A semiflexible polymer is coarse-grained to generate a model of discrete links, length ℓ with tangents $\vec{t}_i$ and bend angles θ_i. **Panel B:** An AFM image of DNA equilibrated to mica is shown. Figures originally published in [93] 15

3.4 **Panel A: Transcriptional regulation.** Lac-repressor-mediated DNA loop formed during repression of the *lac* operon in *Escherichia coli*. **Panel B: Nucleosome formation.** DNA tightly wraps the histone octamer to form a nucleosome, the fundamental building block of chromatin structure in eukaryotic cells. **Panel C: Viral DNA packaging.** Roughly 20 kb of DNA packed in the protein-capsid head of the bacteriophage phi29. (Figure from Ref. [33].) 19

3.3 **Panel A: DNA cyclization J factor.** At long contour length, there is an excellent match between the measured and predicted J factors. At short contour lengths, there are significant differences between the LSEC and the WLC models. The Cloutier and Widom measurements (CW) show much better agreement with the prediction of the LSEC model. **Panel B: DNA bending energy from mica.** For short contour length, there is a much better match to the LSEC model than to the WLC model. At longer contour length the models make identical predictions. Figures originally appeared in reference [93]. 20

4.1 Wide-field pulsed magnetic imaging using an NV ensemble. (a) NV electronic energy level diagram showing the ground, excited spin states ($|m_s = 0\rangle$,$|m_s = \pm 1\rangle$), singlet states, optical excitation (green arrow), emitted photoluminescence (red arrows), and spin-selective, non-radiative inter-system-crossing (gray arrows). (b) Schematic showing 50 nm ferromagnetic nanoparticles adhered to the diamond surface. The magnetic moments of the particles are oriented randomly. The 150 nm NV layer (pink) is fabricated on top of the diamond substrate (gray), and a single NV pointed along the (111) orientation is shown (red). (c) NV ground state energy level diagram showing the zero-field splitting (D), Zeeman splitting of the $|m_s = \pm 1\rangle$ states ($2\gamma_{\mathrm{NV}}\hat{z}_{\mathrm{NV}} \cdot \vec{B}$), and ^{15}N-NV hyperfine splitting (3.05 MHz). RF excitation (orange and blue arrows) rotates the NV spin between the $|m_s = 0\rangle$ and $|m_s = \pm 1\rangle$ states. Two-tone RF excitation is simultaneously driven over the two ^{15}N-NV hyperfine transitions to produce a single combined resonance for each NV electron spin state ($|m_s = \pm 1\rangle$). (d) Laser and multi-tone RF π-pulses are repeated throughout the camera exposure to facilitate wide-field imaging. (e) A Lorentzian-shaped reduction in NV PL is observed when a RF scan is performed through each spin-transition frequency. The resonances are Zeeman split by the external magnetic field. The outer (inner) inflection points f_1, f_4 (f_2, f_3) are denoted by black squares (circles). For the resonance curves shown, the FWHM linewidth $\delta\nu = 300$ kHz and fractional optical contrast $C = 0.03$, with optical pulse = 500 ns, RF pulse = 3500 ns, photon collection rate = 1.1×10^7 Hz from a 1 μm^2 pixel (0.15 μm^3 voxel), and integration time per data point = 144 ms. 23

4.2 Multiple mechanisms lead to changes in NV ODMR on a micron scale when imaging static magnetic dipole and strain fields. (a) Resonance frequency ν shifts due to magnetic field and crystal strain. (b) The FWHM linewidth $\delta\nu$ varies due to gradients of magnetic and strain fields that inhomogenously broaden the NV ODMR in each pixel. (c) Optical contrast C also varies due to due to inhomogenous broadening of the NV ODMR. 25

4.3 Competing magnetic imaging modalities. (a) 'True' static magnetic field projection map generated with the frequency scanning technique outlined in the above Static Magnetic Imaging Modality section (acquisition time 12 s). (b) Single quantum difference imaging (2.4 s). The signal measured with the SQ DI modality is a convolution of the magnetic and strain fields, which are impossible to separate with a single measurement. (c) Double quantum difference imaging (2.4 s). While the DQ DI modality has reduced the impact from the fields that homogeneously shift the NV centers, the DQ signal is more sensitive to the local contrast and linewidth variations of the NV sensing curves. (d) Double-double quantum difference imaging (2.4 s). An inspection of the competing dynamic imaging schemes (b-d) reveals that both the SQ (b) and DQ (c) schemes are significantly compromised by spurious contrast caused by strain gradients and curve-shape variation, respectively, while the DDQ scheme (d) faithfully approximates the 'true' magnetic field projection (a) with a decreased acquisition time. 31

4.4 DDQ imaging of the reorientation of a DNA-tethered magnetic nanoparticle under applied flow. In each panel, the observed DDQ image is compared with a fitted DDQ image (inset) to estimate the magnetic nanoparticle dipole orientation (θ, ϕ), where the NV ensemble symmetry axis is (54.735°, 0°). For all DDQ DI in this figure, a Gaussian smoothing filter with $\sigma = 533$ nm is applied. (a) A time-averaged DDQ DI (8 s) showing initial magnetic nanoparticle orientation before flow. (b) Representative DDQ frames (64 ms of exposure) showing nanoparticle reorientation in response to an applied flow. (c) A time-averaged DDQ DI (8 s) showing the final magnetic nanoparticle orientation with applied flow. 32

5.1 **Panel A: Next-generation magnetic tweezer.** A low-magnitude symmetry-breaking magnetic field is applied at all times. A second tweezer field is used to manipulate the sample. Both the magnitude and direction of the tweezer field are manipulable. **Panel B: DNA-tethered nanoparticles.** Magnetic nanoparticles are functionalized to bind specifically to bio-molecules. **Panel C: Imaging the magnetic field.** A 3-component dipole magnetic field generated by a magnetic nanoparticle is measured at the diamond sensor using the MagPI imaging modality. The plot shows the x and y components of measured magnetic field generated by a nanoparticle. 35

5.2 **Panel A: The micro-torsional balance.** A short-contour-length DNA molecule is tethered at one end to the surface and at the other to a ferromagnetic nanoparticle. Panel A shows an unbent molecule with the bead moment and magnetic field aligned. **Panel B:** The magnetic tweezer is then rotated to generate a torque. The DNA molecule bends to deflection angle θ, where torque balance is achieved and the magnetic and bending torques are equal. **Panel C: Rotation series.** A 2-μm ferromagnetic nanoparticle is tethered by a 100-bp DNA molecule using torsionally-free chemistry. The tweezer magnet is then swept through a 360° rotation and a series of MagPI images were collected. **Panel D: Fit to rotation series.** To determine the orientation of the magnetic nanoparticle, the dipole field is fit to a quantitative image model to infer the moment orientation and the external field orientation. **Panel E: Measured dipole and field orientations.** The inferred dipole moment and field orientations are shown. 35

5.3 **Nano-mechanical torque balance.** (**A**) Diagram of experiment showing top-down view of a single DNA molecule attached at one end to a diamond sensor and to a magnetic nanoparticle probe at the other end. An applied magnetic field reorients the probe magnetic moment. The torque exerted by the applied magnetic field on the probe is balanced by the bending torque exerted by the DNA on the probe. (**B**) Optically-detected-magnetic-resonance (ODMR) of four NV crystallographic orientations is measured across the imaging field of view. The ODMR spectrum contains information about both the applied magnetic field and the probe magnetic field. (**C**) Measured probe magnetic field vector projections, (**D**) fit probe magnetic field projections and (**E**) residuals between measurement and fit. Scale bar is 2 µm. 40

5.4 **Dipole orientation illuminates qualitative differences in DNA binding character, image comparison.** Ferromagnetic probe field images with changing applied field angle are shown for three different biomechanical configurations in the three rows, and different applied field directions in the different columns. In each series, the dipole image is shown, overlaid with the fitted moment direction vector in white and the applied field direction vector in dashed black. (**A**) Particle tethered by an free DNA tether. The dipole moment is free to re-orient and points along the applied field direction. (**B**) Particle stuck to the diamond sensor surface. The dipole moment direction is independent of applied field angle and points in a constant direction. (**C**) Probe in a nano-mechanical torque balance. The probe moment direction is balanced by a torque from the applied field and a torque from the DNA. The particle aligns with the field for certain angles of the magnetic field and deviates from the applied field from other angles due to the torque applied by the DNA. 42

5.5 **Response of dipole to applied field measures bend stiffness.** (a) Control experiments: stuck and free particles. The measured magnetic moment in plane angle ϕ_m is plotted as a function of applied field angle ϕ_B . In the stuck case, the dipole direction is constant and independent of applied field direction. In the free case, the dipole direction tracks with applied field. (b) Torque balance response for 600 bp DNA molecules. Three different particles with three different moment magnitudes m_i are shown. The data is consistent with a WLC sinusoidal model with L_p=150 bp. 43

6.1 Plots of all three components of a measured magnetic field and corresponding least squares fit. Top row: measured magnetic fields. Second row: measured magnetic field after applying gradient mask. Mask determined with method outline in Section 6.3. Third row: simulated magnetic field after applying gradient mask. Fourth row: simulated magnetic field without mask. Fifth row: residual without mask. Sixth row: residual with mask. 52

6.2 Left: Plots of PL counts vs applied RF for pixels with low and high magnetic field gradient. Center: plot of variance of PL counts vs applied RF around a magnetic bead. Right: Plots of detected resonance frequencies with and without pixels masked for having too low variance (corresponding to large magnetic gradient). 53

7.1 **Panel A: Nucleosome sequence preferences.** There is a preference for dinucleotides steps that occur periodically with the DNA helical repeat and are known to facilitate sharp bending of DNA around the nucleosome. These include ≈10-bp periodic AA, TT or TA dinucleotides that oscillate in phase with each other and localize on the histone so that bending occurs into the minor groove of the helix. These repeats are out of phase with ≈10-bp periodic GC dinucleotides, located where the major groove faces histone. The figure was taken from Ref. [81]. **Panel B: Clockwise bending of a 94mer.** When the 94mer is bent in the clockwise direction, soft base steps bend towards the minor groove. When the 94mer is bent in the counter-clockwise direction, GC base steps bend towards the minor groove. **Panel C: Putative anisotropic bending of DNA.** Bending into the minor groove may be energetically favorable at soft dinucleotide steps. 58

Chapter 1

Introduction

1.1 Introduction

Studying the properties of molecules has been, and continues to be, an extremely broad area of research. Under the umbrella of molecular structure and molecular properties, a significant motivator for selection of particular molecule to study is life. After identifying proteins and complexes and polymers with *in vivo* that are involved in biological processes, it is common to isolate these outside of the cell and conduct in vitro experiments to attempt to more directly measure their properties outside of the complex environment of the cell. With the molecule of interest isolated, it is possible to conduct a variety of measurements on it that would be impossible inside the cell. There remains a tension between these two classes of experiments, however, in that the most relevant properties of these molecules of interest relate directly to how they act inside the cell. Thus, *in vitro* experiments are often designed to both mimic biological conditions as best as possible with regards to various environmental conditions (temperature, salinity, crowding etc.) and measure as fundamental of a property of the underlying molecule as possible. The fewer higher order interactions, or levels of abstraction from measurement to implication on biological process, the more directly the measurement can be used to change understanding of how the molecule of interest behaves inside the cell.

Another division in types of measurement (aside from *in vivo* and *in vitro*) is the divide between single molecule and ensemble measurement. Ensemble measurement involves making a measurement on a large group of molecule simultaneously. Aggregating the signal from many individual molecules. A common

example of this is using gel electrophoresis to compare a sample of DNA (which often contains on the order of 10^{11} individual strands of DNA) to a standardized "ladder" to (roughly) measure the length of the strands which comprise the sample. Due to the nature of the readout in this experiment, it would be beyond unfeasible to make this measurement on a single molecule. But, by leveraging the power of measuring all of these molecules simultaneously, it makes running a gel one of the simplest, cheapest, and most consistent bench top experiments one can run. Single molecule measurements, conversely, and eponymously, investigate individual molecules with each measurement. Due to the size of individual molecules, these involve microscopy at some stage. Unlike their ensemble measurement counterparts, single molecule measurements become subject to many more signal to noise issues. There is the constant of microscopy: can the imaging target be resolved above relevant sources of background, but there is also an insidious second question: is the signal being observed truly coming from the single molecule-sensor system that is trying to be observed. Again due to the size of molecules, single molecule samples are often not generated one molecule at a time. Instead, large quantities of individual components are combined, often sequentially, to generate many complexes that can then be brought into an imaging environment. Unfortunately, due to the stochastic nature of the generation of complexes and the scale of Van der Waals forces, many single molecule protocols require a verification step to show that what is being observed is, in fact, the molecule-sensor complex of note, and not a compromised version.

Among single molecule measurements, it is common that the molecule of interest is not directly imaged in the microscopy step. This can be due to the size of the molecule being below the resolvable limit, or the structure of the molecule being incompatible with light reflection or significant refraction compared to the environment. Instead, the molecule is either engineered to have an additional, more visible component (e.g. modifying the DNA inside of single-cell bacteria to attach a fluorescent protein to a protein of interest) or attached to an object that is more easily resolvable in microscopy (e.g. tethered particle motion (TPM) experiments where a polystyrene bead is attached to the end of a DNA molecule that is attached to a cover slip). Most of these more-visible modifications are rotationally symmetric, which poses no limitations when the desired measurement requires only the position of the probe. A variety of measurements of interest in biological systems and of biologically relevant proteins involve orientation (or relative orientation) in addition to position.

This thesis presents advancements in the use of magnetic imaging to facilitate single molecule measurements of orientation and position. The magnetic dipole of a ferromagnetic particle naturally breaks the spherical particle's rotational symmetry. By leveraging the magnetic sensing capability of nitrogen vacancy centers (NVs) in a widefield capacity, imaging the vector magnetic field is possible. Due to the many constraints on magnetic fields laid out in Maxwell's equations, analysis of an image of the magnetic field from a dipole particle allows for inference on the position and orientation of the dipole that generated the field measured. This thesis presents two use cases for this newly developed magnetic imaging system. Both cases use DNA as the underlying biological system, because despite its fundamental nature as a biological relevant molecule that has been studied extensively, these approaches demonstrate the potential for novel measurements of its properties. First, a novel magnetic imaging protocol is presented for video-rate magnetic imaging. This allows for dynamic imaging of a magnetic particle attached to the end of a single DNA molecule, capturing position and orientation information about the end of the DNA molecule on short (30 ms) time scales. Ideally a passive measurement, the exact structure of our magnetic imaging involves an external magnetic field that limits the biological applicability in its current form, and a proof of principle reorientation measurement is presented. Switching to an active measurement to convert the detriment of an external field to a positive, the concept of a magnetic torque balance is combined with DNA tethered particle motion methodology. After attaching a magnetic bead to the end of a short piece of DNA that is attached to the sensing surface, applied magnetic fields attempt to reorient the bead. By reading out the magnetic field generated, and combining the vector magnetic moment measurement of the bead with the measurement of the applied field, a magnetic torque on the bead is measured. Due to the only other torque on the bead being generated by its connection with the DNA, the torque exerted by the DNA is measured as being equivalent to the magnetic torque. This first time measurement of single DNA molecule bend stiffness agrees with existing techniques, and presents an approach for exploring various DNA bend stiffness dependencies and probing unexplored phase space in DNA length-bend response space.

1.2 Challenges and Approaches

As is common in technique development, there are a wide variety of challenges addressed in this thesis. They include:

- modification of existing biological sample prep and imaging protocols to be compatible with newly introduced sensing tools

- interpretation and simulation of expected magnetic field signal under experimental conditions to infer underlying probe parameters

- extensions of existing imaging protocols to mitigate sensitivity loss due to novel, wide-field, rapid, magnetic imaging

1.3 Outline

This thesis begins by motivating the development of a magnetic imaging platform on a microscopic scale for use in biological experiments in Chapter 2. Additionally, it discusses the choice of candidate system used for benchmarking and displaying feasibility of the magnetic imaging platform. Chapter 3 provides relevant background for both the biological systems discussed in later sections, and the magnetic imaging platform. Chapter 4 demonstrates a novel quantum control scheme for rapid magnetic field imaging, as well a proof of principle experiment. Chapter 5 provides an experimental description and presentation of preliminary results in a novel, single-molecule, DNA bend stiffness measurement. Chapter 7 summarizes the thesis while providing potential future applications of the magnetic imaging platform, some direct extensions of work presented. Finally, in Appendix A a variety of relevant biological protocols for the experiments conducted are presented.

Chapter 2

Motivation

2.1 Introduction

In this chapter, the general motivation for development of a magnetic-particle-imaging platform (magPI) is discussed. Additionally, the use of DNA (and various experiments designed around it) as a testing system is defended.

2.2 Advantages of a single-molecule biological assay that is unbleachable and measures position and orientation.

In the field of single-molecule biophysics, the imaging and tracking of various proteins or pieces of biological material, both in vivo and in vitro, allows for a more complete understanding of how living things function. There are a variety of methods for tracking individual molecules (fluorescent protein or antibody attachments), and determining the proximity of those molecules to other parts of the cell or system [15]. Some of these are static measurements that tell us about structure, while others probe the dynamics of isolated systems or living cells. As all of the above techniques rely on fluorescent molecules of one kind or another, they are all subject to bleaching of those fluors, and the relative rotation of the roughly isotropic radiation of the fluors does not give any information. There are, of course, other assays that get around bleaching quite nicely. A common form of these is attaching a bead to a system of interest and using white light imaging to image the movement of the bead. Because the bead is attached to the system, one can work

backwards from its motion to some model of the underlying system. Additionally, because it does not rely on a fluorescent molecule, you can take long time lapses of very short exposures without worrying about the fidelity of the technique. To accurately measure the location of the bead, there are a variety of image processing techniques, but they all boil down to using the full point spread function (PSF) of the bead to achieve sub-diffraction-limit resolution on the location of the center of the bead. These experiments still have a common issue with the fluorescent-probe-based imaging assays in that the bead that is attached to the end is often (roughly) spherical. This means that this method cannot directly measure out the orientation of the system that it is attached to. To get around this, there are examples of attaching beads in a way that their translational motion corresponds to a rotation of the system ([47]) and there are even examples of using oblong or distorted beads to be able to measure the rotation of the particle (paper with 3d xyz and rotation stuff). A major issue with both of these methods is that they are heavily dependent on the system being amenable to how the bead is attached or require specific calibration for the attached oblong particle (as the shape is hard to precisely measure or generate many particles the same way when they are oblong).

In order to obtain orientation information about an attached particle, all one needs is a method to break the rotational symmetry of that particle. Ideally, this would be one where the anisotropy can still be observed as the probe particle gets shrunk down to as small a size as possible (the smaller the probe is, the less influence it has on the dynamics of the combined biological system-particle that is being observed). One property that is already used in many biological assays that can be used in this context is beads with magnetic fields. Already used in the separating of material by functionalizing the outside of them and using a magnetic field to separate the beads, there exist many commercially available micron and sub-micron scale magnetic beads [38]. In previous studies that have all used white light imaging of non-magnetic beads, if there was a way to measure the vector magnetic moment of that bead, the entirety of the data set could be expanded by including the relative orientation of the bead between images in addition to the location.

2.3 Why DNA is a good candidate for orientation dependent measurements

In addition to its biological relevance, DNA mechanics plays another important role in the context of biophysics: It is an exceedingly tractable proving ground for understanding the interplay between structure and function in a biological context. Consider two other examples of linear biopolymers: single-stranded nucleic

acids (*e.g.* mRNA) [51] and polymers of amino acids (*i.e.* proteins) [18]. In both cases, the complexity of the free energy landscape makes predicting tertiary structure from primary structure challenging. In contrast, the structure of dsDNA is so highly predictable that DNA is the basis for molecular-scale design in the context of DNA origami [99; 94] and its configurational statistics are tractable, sometimes even analytically, using statistical mechanics [28]. For instance, the nearly perfect success of Marko and Siggia in predicting the force-extension curve of dsDNA measured for a single molecule by Bustamante was a great triumph of both single-molecule manipulation on the experimental side and quantitative prediction on the theoretical side [54; 13]. The more recent failures of these same models and systems in the context of the cyclization of short-contour-length DNA molecules therefore present a mystery that is both biologically relevant and biophysically compelling [14; 86].

More specifically, the extension to using a magnetic bead (and magnetic imaging platform) is nautral from the space of Tethered Particle Motion (TPM) experiments.

Chapter 3

Background

3.1 Magnetic field sensing

3.1.1 Optically detected magnetic resonance in Nitrogen Vacancy Centers in Diamond

Nitrogen vacancy (NV) centers in diamond are a point defect with a very useful electronic energy level structure. This section will outline the relevant background for the manipulation of NV centers in diamond to do wide-field magnetic imaging.

We begin with the Hamiltonian of the NV center. The spin states of the two electrons in the NV- center determine the energy splitting (seen in the Jablonski diagram of the NV center point defect).

In addition to being slightly higher energy than their $|s = 1, m_s = 0 >$ counterparts, the ground and excited state energy levels for the $|s = 1, m_s = +1 >$ and $|s = 1, m_s = -1 >$ are degenerate if there is no magnetic field present. Interestingly, the energy gap between the ground and excited states of all three m_s values are of equal magnitude. When excited with a green laser (532 nm) from their ground state to their excited state, each of these three m_s value states will decay back down to their respective ground state and emit in the near IR (630 nm - 800 nm). In addition to this bright channel, the states where $|m_s| = 1$ can also decay down to the ground state of $m_s = 0$ with a dark channel. These decays may emit several photons in a multi-step decay process, but as they do not emit in the visible red range, they can be filtered separately. Some relevant numbers for this process: for a single NV center in ideal conditions the rate at which the $|m_s| = 1$ excited states will undergo the dark transition to the $m_s = 0$ ground state is 30 percent,

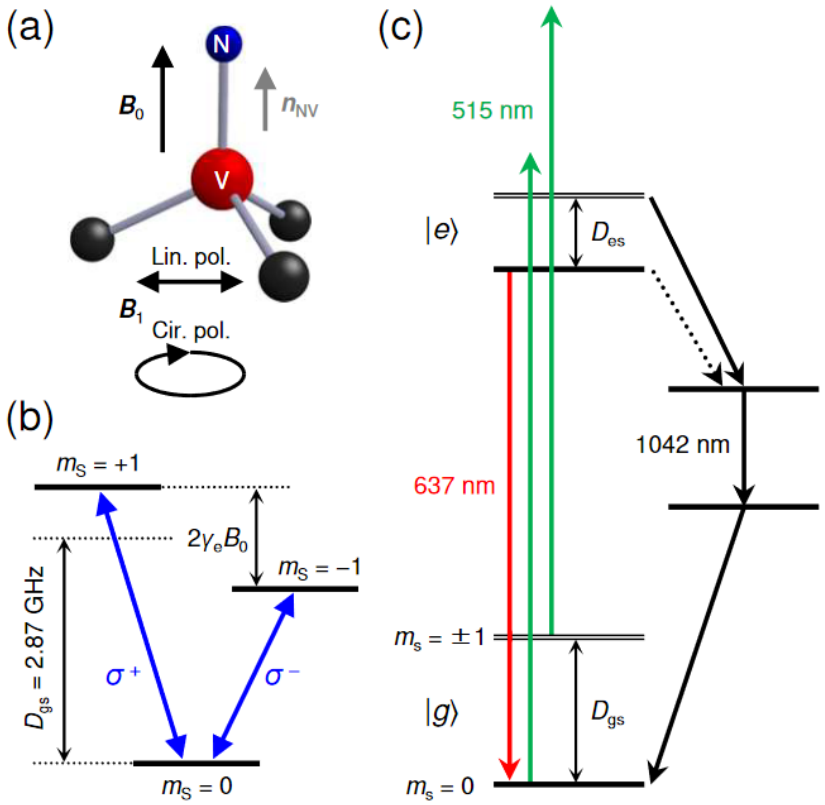

Figure 3.1: (a) Schematic of NV center. Circularly polarized light can be used to select for one possible transition, while linear polarized light allows for both. (b) Ground state of the NV center system for available z-spin projections. Zero field splitting and Zeeman shift denoted. Required polarization helicity indicated for transitions (c) Energy level diagram showing excited states for states in (b) as well as singlet states for non-radiative decay from $m = \pm 1$ excited states. Green arrows indicate the excitation to higher phononic sidebands. Red arrows indicate emission upon direct decay to ground state. There is an unlabeled emission transition from the excited to ground state for $m = \pm 1$ as well. Figure originally from [1]

the lifetime of the bright decay is 10 ns and the lifetime of the dark decay is 300 ns. All of this allows for reading out of the spin state of an NV center if isolated, or the reading out of the percentage of an NV population in a given spin state. For bulk spin state detection, one would excite with a 532 nm laser and collect in the 630-800nm regime and look at the relative intensity curve of the 800 nm regime as a function of excitation time. Because the $|m_s| = 1$ states can decay back into the $m_s = 0$ ground state but the $m_s = 0$ ground state cannot switch over to the $|m_s| = 1$ under these conditions, the relative intensity will have the form $1 - pe^{(-t\tau)}$ where p is the initial fraction of NV centers in a $|m_s| = 1$ state, and tau is the decay constant controlled by the rate at which the states oscillate between ground and excited and the rate at which

the $|m_s| = 1$ decay back into the $m_s = 0$ ground state. This optical detection of spin readout will be integral for determining local magnetic field.

Shifting to look just at the ground state of the $m_s = 0$ and $|m_s| = 1$ states ((b) of Fig. 3.1). By applying a well chosen (further description to come) radio frequency field, the $m_s = 0$ state can be rotated into an $m_s = +1$ or $m_s = -1$ state. Importantly, the radio frequency that provides optimal pumping from the $m_s = 0$ ground state to the $|m_s| = 1$ ground states is controlled by the energy difference between the two levels. Optimal selection of other parameters of the applied RF pulse can be found in [8]. As mentioned above, the spacing between $m_s = 0$ and $m_s = 1$ is the same as $m_s = 0$ and $m_s = -1$ in the absence of a magnetic field. But, due to the Zeeman shifts' dependence on the sign of the m_s value, when the NV center sits in an external magnetic field, the two $|m_s| = 1$ ground states split from each other. This changes the energy gap from the $m_s = 0$ ground state to both of the $|m_s| = 1$ ground states. This allows for a readout of the local magnetic field from the optical response of selectively rotated NV centers. There are a variety of control methods for getting out magnetic field information from NV centers, but this thesis will focus on two classes of measurement meant for DC or time dependent DC fields (AC field sensing with NV centers describes sensing oscillatory fields specifically). The most intuitive method of detecting a magnetic fields with NV center manipulation is by taking a series of collections: applying a specific radio frequency to rotate the $m_s = 0$ ground state to one of the $|m_s| = 1$ ground states and reading out the number of photons after exciting with green laser. Again, because the percentage of the NV population that rotates is dependent on how closely the applied radio frequency corresponds to the energy gap between the $m_s = 0$ ground state and the $|m_s| = 1$ ground states, the number of photons collected will be at a minimum when the radio frequency matches exactly, and fall of as a lorentzian around it. By reading out the energy gap between the $m_s = 0$ ground state and either of the $|m_s| = 1$ ground states, you can determine how much the $|m_s| = 1$ ground state has shifted. Unfortunately, there are myriad parameters that impact this (as seen in the Hamiltonian). Temperature, crystal strain, and electric field all affect the energy gap from the $m_s = 0$ ground state to the $|m_s| = 1$ ground states, in addition to the magnetic field. Usefully, as seen in the Hamiltonian, all of the non-magnetic shifts of the NV energy levels depend on spin squared operators. Because $|m_s| = 1$ spin states all have the same eigenvalues for all spin-squared operators, the energy gap from the $m_s = 0$ ground state to the $|m_s| = 1$ ground states are changed by the same amount. Because the Zeeman shift on the energy levels

depends on a linear spin operator, it shifts the $|m_s| = 1$ ground states anti-symmetrically! This allows for what has now been dubbed a "Double Quantum" approach. By scanning over a wide range of frequencies and finding the location of the resonances from the $m_s = 0$ ground state to both of the $|m_s| = 1$ ground states, one can subtract the two energy gaps to find what the energy difference is between the $m_s = +1$ ground state and the $m_s = -1$ ground state. This energy gap being only influenced by the magnetic field gives a readout of the local magnetic field at the location of the NV centers.

An inherent issue with this method is the number of applied radio frequencies required. For optimal sensitivity, it is useful to keep the NV center optically detected magnetic resonance (ODMR) linewidths as narrow as possible, but to accurately find the resonant frequency for the ODMR curve, several points are required for each curve! There are also intensity based approaches for extracting spin-state information that will be discussed later.

Thus far, the discussion of has approached using an ensemble of NV centers in concert to map the magnetic field. All of these calculations assume that the magnetic field over the grouping of NV centers (which we can suggestively label as a single pixel) is slowly enough varying that the resonances for the different NV centers are not split by a large margin. Theoretically, if the magnetic field being imaged varies significantly over a single pixel, you would have multiple sets of resonances corresponding to the same quantum states in NV centers experiencing a sufficiently different local magnetic field. The NV full pixel response is only usable if the gradient is sufficiently small, this will be discussed further in Chatper 6.

As mentioned earlier, the maximum contrast a single NV center has when the applied RF is on resonance is 30 percent. This comes from the branching ratio of the decay paths and the two lifetimes of the bright and dark decay pathways of 10 ns and 300 ns respectively. The linewidth of the ODMR response however, is impacted by many experiment specific parameters. Both of these are further impacted by the fact that the curves we are generating for each pixel have 300-1200 NV centers in them, all of whose signals are being added together. When looking at the shape of the NV response curve for a single pixel, it is really those 300-1200 PL response curves overlapped. Because the orientations in the sample are randomized there is unavoidable variation in the effective contrast across a the diamond. In the diamond samples used for the data presented in this thesis, the NV density is 10^{17} NV's/cm^3. The reduction in contrast seen from the 4 orientations, and the hyperfine splitting, leave 3% contrast the optimal expected contrast for a pixel in

widefield NV sensing.

Widefield imaging involves following the above procedure across a diamond chip and image the surface of the chip with a 100x objective. This allows for localization the NV response to 500 nm pixels, reading out the magnetic field in each pixel separately. This does require a certain degree of fidelity in the NV sensing chip as well as in the laser (excitation) and radio frequencies applied (to rotate the spin states). The laser is guided through the backside of the objective and focused onto the sensing layer of the NV chip. Focusing the laser spot and expanding it, an effective sensing area of 10 um x 10 um is generated. While not entirely uniform, within this regime the intensity is within a factor of 2, which is small enough to not create larger noise issues with laser power fluctuations. The radio frequencies are applied by a radio cavity that is placed on the other side of the NV chip from the objective. The microscope is set up so that the center of the resonant cavity for applying radio frequencies is lined up with the center of the objective, and the sample can move independently of both of them. Because the output of the cavity is highly dependent on the position relative to the cavity, this minimizes the impact of the cavities non-isotropic radiative properties.

3.1.2 Going from magnetic field measurement to magnetic bead parameterization

It is important to note that the actual end observation will be of the nature of the position and orientation of the biological system under the experimental conditions. Just measuring the magnetic field of the bead attached to the system is insufficient to make comments on the dynamics (or statics) of a biological system. Thus, once the magnetic field of the particle attached to the biological system of interest has been imaged, we have to work out the position and orientation of the bead that generated this magnetic field. Before diving into this, a quick argument why it is, in fact, possible. Previous work has been done for calculating the magnetic field in a sourceless plane in the context of geology measurements [52], but for a more brief proof consider the following. For a sourceless region, the lack of divergence or curl of a magnetic field gives two differential equations looking for the 3 terms of the magnetic field and their integration constants. Knowing a single projection of the magnetic field is then enough to reduce the number of unknowns to two, and the system is solvable. Thus, knowing just a single projection of the magnetic field in the plane is sufficient to find the total magnetic field. This magnetic field corresponds to a single possible orientation and position of the magnetic moment of the bead. Assume, for sake of contradiction, that there are two

possible sets of orientation, position, and moment magnitude data that generate the same exact magnetic field. Flip one of them. The magnetic field in the entirety of the plane due to those two magnetic dipoles now vanishes. This means derivatives of the components of the magnetic field in the plane vanish. To maintain a divergenceless magnetic field, the derivative of the component perpendicular to the plane must also vanish. This corresponds to a constant magnetic field in all space due to these two beads of zero (because we are assuming it was zero in the plane). The only way for two magnetic dipoles to completely cancel each other's magnetic fields out in all space is if they are at the same location with opposite signed magnetic moments. If they are not on top of each other, it is impossible for the field to vanish as you get sufficiently close to both of them. The uniqueness of solution is also guaranteed by the uniqueness of solutions to Poisson's equation. the measuring of the magnetic field in the plane of the sensor corresponds to determining the Neumann boundary conditions for the magnetic scalar potential generated by the magnetic dipole.

3.2 Biological background on relevant DNA dynamics for the experiments presented.

Understanding the dynamics of how DNA interacts both with complexes within the cell and with itself are ongoing research questions for a complete picture of how cells function. The ubiquity of the double-helical molecule in all life leads to many interesting interactions. There are examples from viruses to bacteria to humans of the short-length bending dynamics being significant in functionality. [1]

3.2.1 Existing Models of DNA Mechanics and Experimental Approaches

Quantitative models for DNA statistics.

To construct a quantitative model for DNA conformation, we coarse-grain the polymer configuration into length ℓ segments, each with unit tangent $\vec{t}_i$. The fundamental quantitative basis for an effective model of DNA bending is the bend energy defined on contour-length scale ℓ [91]. The bend energy for the molecule

[1] A version of the following sections in this chapter came from a grant proposal created by :
Paul A. Wiggins, Kai-Mei C. Fu, Zeeshawn Kazi, and Isaac Shelby

is expressed as:

$$U = \sum_i U(\theta_i), \tag{3.1}$$

where $U(\theta_i)$ is the bending energy associated with the bend angle θ_i between successive links i and $i+1$, as shown in Fig. 3.2A. In an elastic model (*i.e.* a Hookean model), the bending energy is quadratic in the deflection angle θ_i:

$$U(\theta_i) = \frac{1}{2}\kappa\theta_i^2, \tag{3.2}$$

where $\kappa = k_B T \xi/\ell$ is the bending modulus of the link, $k_B T$ is the Boltzmann constant times temperature and ξ is the persistence length. When this elastic model is used to describe the configuration of a molecule in the canonical ensemble (in the continuum limit), this model is called the Worm-Like Chain model (WLC).

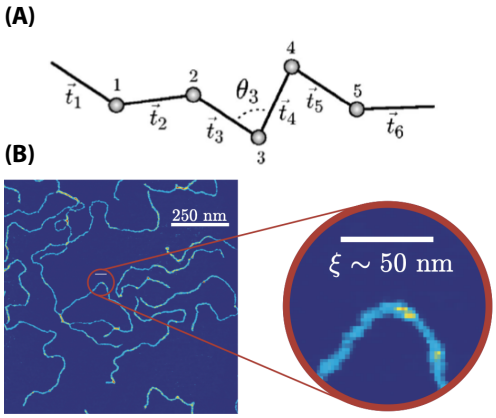

[ht]

Figure 3.2: Panel A: An effective model for DNA mechanics. A semiflexible polymer is coarse-grained to generate a model of discrete links, length ℓ with tangents $\vec{t}_i$ and bend angles θ_i. **Panel B:** An AFM image of DNA equilibrated to mica is shown. Figures originally published in [93]

DNA conformational statistics. To understand the limitations of current knowledge of DNA mechanics, it is important to understand that there are two different bending regimes described by distinct physical properties of the DNA molecule. On length scales much longer than the persistence length, $\xi \approx 50$ nm (150 bp), DNA is efficiently bent by thermal fluctuations and entropy dominate the DNA statistics. (See Fig. 3.2B.) In the context of experiments that probe these scales, the Renormalization Group ensures that the only relevant parameter describing the configurations is the persistence length [91]. Experiments like force-extension, SAXS [55], and long-contour-length cyclization experiments [76; 59; 88; 89; 77; 16; 37] all fall into this category. These experiments are predicted to be precisely described by the WLC; however, the precise match between theory and experiment in this regime is no guarantee of success in describing tightly-bent DNA configurations since competing models with vastly different short-length-scale behavior can none-the-less have the same persistence length and therefore result in the same long-length-scale behavior [91].

Cyclization. For length scales shorter than a persistence length, the dominant determinant of the DNA configuration is the bending energy. (See Fig. 3.2B.) It is perhaps intuitively obvious that experiments that wish to probe the mechanics of tightly-bent DNA should do just that: measure observables that are dominated by DNA molecules in these tightly-bent configurations. The DNA cyclization assay can be performed for short DNA molecules. Cyclization measures the effective concentration, the J factor (J), of one end at the other with the correct orientation for ligation. J is a particularly convenient observable since in can be computed theoretically and depends only on DNA mechanics [76; 59; 88; 89; 77; 16; 37].

The difficulty with J. There are two significant shortcomings with DNA cyclization experiments. The first problem is that DNA cyclization measurements do not directly measure the DNA bending energy [76; 96]. The issue is as follows: The quantity that is measured in the cyclization measurement is the J factor, proportional to the probability density that the end-to-end displacement is zero and the tangent and DNA twist are suitably aligned for ligation. This amplitude is computed by path integral over all configurations in the canonical ensemble with delta-function constraints enforcing the configuration [76; 96]. These delta functions lead to highly non-trivial contributions to J and therefore it is very difficult to solve the *inverse problem*: Given a set of J factor measurements, what is the bending energy? In summary, the bending energy determines J but J does not directly determine the bending energy.

The second significant complication with cyclization is experimental in nature. There is an unresolved debate in the community about the reported value for the J factor in the 100-bp regime. Widom and coworkers reported orders-of-magnitude discrepancies with the WLC model at 90-100 bp [14]; however, a year later, Vologodskii and coworkers disputed these claims [23]. (See Fig. 3.3B.) Although Ha and coworkers have subsequently developed a ligase-free assay that seems to measure J factors consistent with Widom et al [86], many questions remain about both the strength of the experimental evidence as well as systematic questions about the meaning of the assay for short-contour-length molecules [90].

Direct measurement of the bending energy by AFM imaging. Due to the small physical scale of the DNA persistence length, there have been relatively few attempts to directly measure the bending energy. One approach is to immobilize and equilibrate DNA on mica then resolve the surface-bound conformations by atomic force microscopy (AFM) [71]. The first measurements of DNA statistics on mica demonstrated

that the predicted solution persistence length was consistent with the known solution persistence length [71]. High-resolution bending energy measurements did resolve anomalous bending with enough softening at high curvature to account for the observed anomalous cyclization and these measurements were used to formulate a new empirical DNA bending model: the (Linear) Sub-Elastic Chain model (LSEC) [93]. (See Fig. 3.3A.) However, these experiments also have some important flaws: They rely on the critical assumption that the configurational statistics of DNA adsorbed to mica is equivalent to those of DNA in solution, and questions have been raised about whether these observations could be an AFM imaging artifact [57; 56]. *It is therefore important to develop another independent method to measure the bend energy of short-contour-length DNA molecules.*

3.2.2 DNA looping: biological relevance and model defying measurements

Tightly-bent DNA is found in many biological contexts: DNA wraps histones to form nucleosomes, it forms DNA loops in transcriptional regulation and it is tightly spooled in the heads of bacteriophages. In each of these cases, the fundamental mechanical properties of DNA play a central role in the biological mechanism. However, in spite of its biological significance, there have been no measurements that directly probe the torque versus bend angle of the molecule. Furthermore, studies of DNA-histone affinity reveal that the bend modulus of DNA is both sequence-dependent and that this sequence specificity plays a central role in determining the positioning of the nucleosomes on the eukaryotic genome, itself a central player in gene regulation.

The biological significance of tightly-bent DNA. Double-stranded DNA (dsDNA), the central repository of biological information, is a long linear semiflexible polymer [4; 33]. In all biological systems, the contour length of the DNA genome is much larger than the physical size of the cell, nucleus or capsid that contains it. Thermal fluctuations alone significantly condense the DNA, but its volume must be decreased by at least three-orders-of-magnitude in order to result in its physiological structure: the chromosome [68]. However, condensation is just one role of the complex biological machinery that shapes the chromosome. While condensed, the chromosome is simultaneously replicated, transcribed and partitioned as the organism proliferates [4]. At every stage of these processes, the DNA configuration is manipulated by proteins from transcription factors to polymerases and many of these steps result in DNA bending. Three specific examples

illustrate the surprisingly rich biological significance of DNA bending: (i) In eukaryotic cells, chromatin is formed by tightly wrapping DNA around histone octamer proteins to form nucleosomes [33]. However, not all DNA is equally flexible and biology uses an auxiliary, mechanical language of DNA sequence to position nucleosomes at particular loci on the genome [14; 75; 81]. See Fig. 3.4B. (ii) To infect a bacterium, a bacterial virus (bacteriophage) must deliver its genetic information through the cell wall. Deprived of the canonical biological fuel of ATP, it is the bending energy of the tightly-spooled DNA in the lambda phage head which plays a central role in translocating the viral genome into the host [79; 69; 25]. See Fig. 3.4C. (iii) In the regulation of the *lac* operon, two biological signals are integrated mechanically by the formation of a DNA loop, facilitating the repression of *lac* operon transcription [63; 50]. See Fig. 3.4A. In these three examples, DNA conformation, and more specifically bending on length scales of tens of nanometers, is a central player in the functional mechanism.

Existing measurements of DNA mechanics have so far failed to generate a quantitative model for the bending of double-stranded DNA capable of describing many of the most biologically relevant DNA conformations *in vivo*. The most recent single-molecule cyclization experiments show a two order-of-magnitude mismatch between experiment and the standard model of DNA mechanics: the Wormlike Chain Model (WLC). Furthermore, although both force-extension and cyclization experiments provide highly non-trivial tests of a model of DNA mechanics, neither experimental approach can be understood to *directly* measure the DNA bending energy, which constitutes the central ingredient of a quantitative model of DNA statistical mechanics. For instance, the recently reported large mismatch between experiment and theory suggests flaws in the WLC model, but *does not* reveal how the WLC model should be modified. *These challenges suggest that a new experimental approach is required to make significant progress on this outstanding and fundamental problem in quantitative biology.*

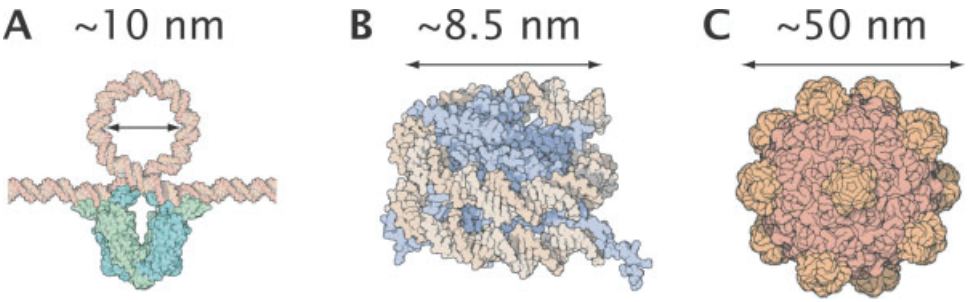

[ht]

Figure 3.4: Panel A: Transcriptional regulation. Lac-repressor-mediated DNA loop formed during repression of the *lac* operon in *Escherichia coli*. **Panel B: Nucleosome formation.** DNA tightly wraps the histone octamer to form a nucleosome, the fundamental building block of chromatin structure in eukaryotic cells. **Panel C: Viral DNA packaging.** Roughly 20 kb of DNA packed in the protein-capsid head of the bacteriophage phi29. (Figure from Ref. [33].)

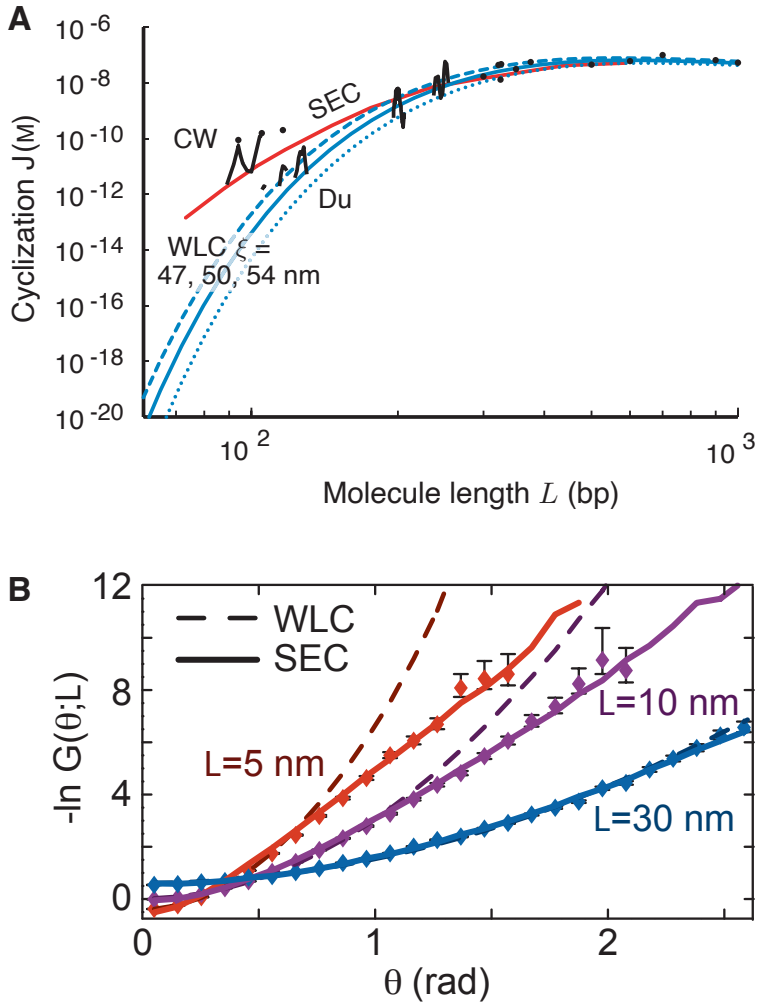

Figure 3.3: Panel A: DNA cyclization J factor. At long contour length, there is an excellent match between the measured and predicted J factors. At short contour lengths, there are significant differences between the LSEC and the WLC models. The Cloutier and Widom measurements (CW) show much better agreement with the prediction of the LSEC model. **Panel B: DNA bending energy from mica.** For short contour length, there is a much better match to the LSEC model than to the WLC model. At longer contour length the models make identical predictions. Figures originally appeared in reference [93].

Chapter 4

Wide-field dynamic magnetic microscopy using double-double quantum driving of a diamond defect ensemble

4.1 Introduction

The success of the negatively-charged nitrogen-vacancy (NV) center in diamond for magnetic field sensing is due to a powerful combination of characteristics: a long spin-coherence time, the ability to perform optically-detected magnetic resonance (ODMR) spectroscopy at room temperature, and a solid-state host environment which facilitates sample-sensor integration [1; 39; 73; 6]. One exciting emerging application is magnetic field imaging using a diamond sensor comprising a diamond substrate with a thin layer of NV centers fabricated at the top surface [48; 83; 7; 43; 74]. In this NV ensemble imaging system, it is critical that the inhomogeneities across the imaging area are eliminated in order to reach the sensitivity floor given by a single-pixel resonance curve. To this end, the NV community has demonstrated many sensor growth and fabrication methods that increase NV density and homogeneity [2; 64; 66; 24; 82; 44], as well as quantum control methods that suppress external-field dependence and increase ensemble spin coherence [9; 62; 53; 17]. In this paper, we expand on these techniques to present a quantum control method compatible with high-frame-rate magnetic-field imaging. Our method, double-double quantum (DDQ) driving, mitigates

inhomogeneities caused by variations of the NV resonance curve. [1]

In NV ensemble ODMR, magnetic fields can be imaged by characterizing the photoluminescence of optically-excited NV centers after probing the NV spin ground states with radio-frequency (RF) π-pulses [Fig. 4.1]. The resonance RF depends on magnetic field because of the Zeeman splitting of the $|m_s = \pm 1\rangle$ NV electronic spin states [1]. However, in addition to sensitivity to magnetic field, the resonances are also perturbed by inhomogeneities in electric field, temperature, and crystal strain [20; 60; 3; 11]. Due to the symmetry of the NV center, these non-magnetic perturbations affect the two NV electron spin resonances ($|m_s = 0\rangle \leftrightarrow |m_s = \pm 1\rangle$) in the same way and can be eliminated by characterizing both resonances [53; 26].

For wide-field magnetic imaging of time-varying fields, the full characterization of the resonance curves is too slow to capture the magnetic-field dynamics in many applications. In these dynamic applications, shifts of one resonance curve can instead be mapped to changes in emitted NV photoluminescence (PL) intensity by applying single-frequency RF excitation [67; 58; 95]. This “single-quantum" (SQ) imaging modality enables partial reconstruction of the local magnetic field with a higher frame-rate. The double-quantum (DQ) modality, which drives both NV electron spin transitions simultaneously by applying a two-tone RF pulse, eliminates pixel-to-pixel non-magnetic perturbations of the transition resonance frequencies [53; 26]. However, variations of the shape of the resonance curve also cause changes in the emitted PL intensity and therefore generate spurious contrast which limits the magnetic sensitivity. These variations arise from inhomogeneities in NV and other paramagnetic spin densities as well as external fields [9], and as shown in this work, can severely limit the utility of the DQ modality for wide-field imaging applications. By expanding to a four-tone DDQ driving scheme, we suppress anomalous contrast due to resonance-curve-shape variations pixel-by-pixel across the field of view. This enables high-frame-rate imaging of time-dependent magnetic fields. We first demonstrate the SQ, DQ, and DDQ imaging modalities by imaging static fields, and show the DDQ signal is linearly proportional to the magnetic field projection along the NV symmetry axis. We then use the DDQ driving technique to image the dynamic magnetic field produced by

[1] A version of this chapter has been published as:
Zeeshawn Kazi, Isaac M. Shelby, Hideyuki Watanabe, Kohei M. Itoh, Vaithiyalingam Shutthanandan, Paul A. Wiggins, and Kai-Mei C. Fu 2021. Wide-Field Dynamic Magnetic Microscopy Using Double- Double Quantum Driving of a Diamond Defect Ensemble. Physical Review Applied, 15, 054032. Copyright 2021 by the American Physical Society. https://doi.org/10.1103/PhysRevApplied.15.054032

a ferromagnetic nanoparticle tethered by a single DNA molecule to the diamond sensor surface.

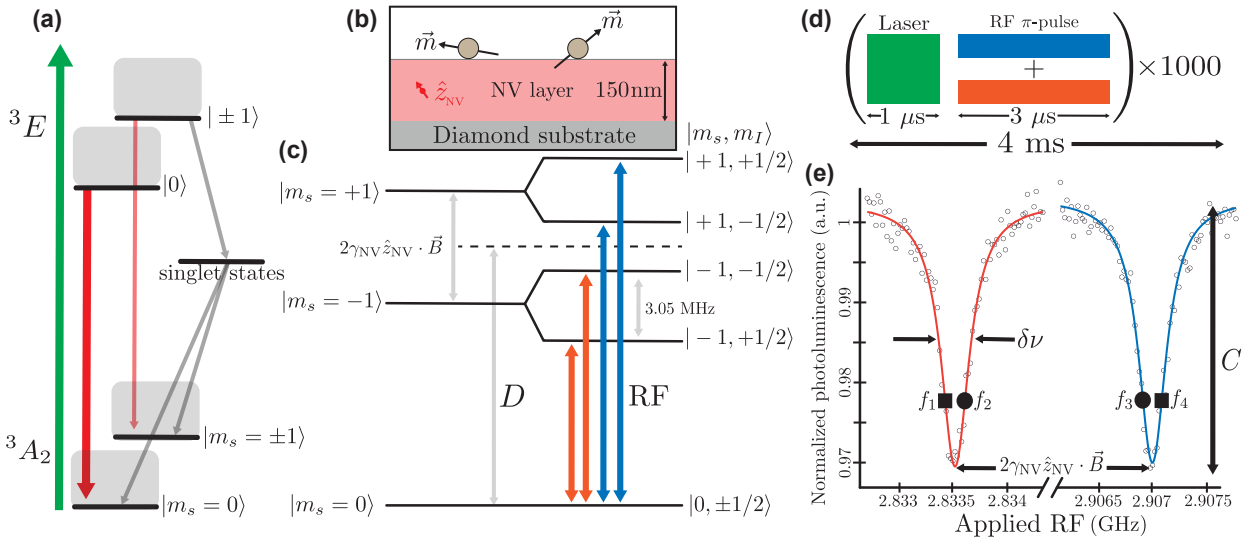

Figure 4.1: Wide-field pulsed magnetic imaging using an NV ensemble. (a) NV electronic energy level diagram showing the ground, excited spin states ($|m_s = 0\rangle$,$|m_s = \pm 1\rangle$), singlet states, optical excitation (green arrow), emitted photoluminescence (red arrows), and spin-selective, non-radiative inter-system-crossing (gray arrows). (b) Schematic showing 50 nm ferromagnetic nanoparticles adhered to the diamond surface. The magnetic moments of the particles are oriented randomly. The 150 nm NV layer (pink) is fabricated on top of the diamond substrate (gray), and a single NV pointed along the (111) orientation is shown (red). (c) NV ground state energy level diagram showing the zero-field splitting (D), Zeeman splitting of the $|m_s = \pm 1\rangle$ states ($2\gamma_{NV}\hat{z}_{NV} \cdot \vec{B}$), and ^{15}N-NV hyperfine splitting (3.05 MHz). RF excitation (orange and blue arrows) rotates the NV spin between the $|m_s = 0\rangle$ and $|m_s = \pm 1\rangle$ states. Two-tone RF excitation is simultaneously driven over the two ^{15}N-NV hyperfine transitions to produce a single combined resonance for each NV electron spin state ($|m_s = \pm 1\rangle$). (d) Laser and multi-tone RF π-pulses are repeated throughout the camera exposure to facilitate wide-field imaging. (e) A Lorentzian-shaped reduction in NV PL is observed when a RF scan is performed through each spin-transition frequency. The resonances are Zeeman split by the external magnetic field. The outer (inner) inflection points f_1, f_4 (f_2, f_3) are denoted by black squares (circles). For the resonance curves shown, the FWHM linewidth $\delta\nu = 300$ kHz and fractional optical contrast $C = 0.03$, with optical pulse = 500 ns, RF pulse = 3500 ns, photon collection rate = 1.1×10^7 Hz from a 1 μm^2 pixel (0.15 μm^3 voxel), and integration time per data point = 144 ms.

4.2 Experimental Methods

The wide-field NV magnetic particle imaging (magPI) platform used in this work utilizes a diamond sensor with a near-surface, high density NV ensemble [Fig. 4.1(b)]. A 150 nm ^{15}N doped, isotope-purified (99.999% ^{12}C) layer was grown by chemical vapor deposition on an electronic-grade diamond substrate (Element Six). The sample was implanted with 25 keV He^+ at a dose of 5×10^{11} ions/cm^2 to form vacan-

cies, followed by a vacuum anneal at 900 °C for 2 hours for NV formation and an anneal in O_2 at 425 °C for 2 hours for charge state stabilization [44]. The resulting ensemble has NV density of 1.7×10^{16} cm^{-3} and ensemble spin coherence time $T_2^* = 2.5$ μs (further details in Supplemental Material [42]).

The NV electronic structure and optical and RF control are summarized in Fig. 4.1. A 532 nm laser pulse is used to optically pump the NV ensemble into the $|m_s = 0\rangle$ triplet ground state. RF excitation drives transitions from this ground state into the $|m_s = \pm 1\rangle$ spin states. Optical excitation from the $|m_s = \pm 1\rangle$ states results in a reduction of PL intensity due to a spin selective, nonradiative inter-system-crossing [32]. This relaxation provides the spin-dependent PL contrast and initialization into the $|m_s = 0\rangle$ state. Monitoring the emitted PL as a function of RF enables measurement of ODMR for each NV ground state spin transition [Fig. 4.1(e)].

From a Lorentzian-shaped resonance curve [see Fig. 4.1(e)], the volume-normalized, shot-noise-limited dc magnetic sensitivity is given by

$$\eta_{SQ}^{V} \approx \frac{1}{\gamma_{\mathrm{NV}}} \frac{\delta\nu}{C} \sqrt{\frac{V}{N}}, \tag{4.1}$$

where C is the optical contrast (fractional depth of the resonance curve), $\delta\nu$ is the full width at half maximum (FWHM) linewidth, γ_{NV} is the NV gyromagnetic ratio (28 MHz/mT), N is the photon detection rate and V is the collection volume [1]. In the magPI platform, the average volume normalized sensitivity $\eta_{SQ}^{V} \approx 31$ nT Hz$^{-1/2}$ μm$^{3/2}$. All three sensor parameters C, $\delta\nu$, and N vary across the imaging field of view.

Optical power broadening of the resonance curve is eliminated by using pulsed excitation in which optical and RF fields are applied separately [21]. Optical pulses and RF π-pulses (both μs-scale) are applied to the ensemble repeatedly to fill a sCMOS camera exposure (ms-scale). Each camera exposure is taken with a single set of RFs with a fixed pulse duration [Fig. 4.1(d)], enabling pulsed NV ensemble control and readout with wide-field camera exposure times [80].

RF excitation is delivered via a broadband microwave antenna with transmission resonance at the NV zero-field-splitting D [72]. Each RF applied is mixed to create two equal tones separated by 3.05 MHz, which enables simultaneous driving of the two ^{15}N-NV hyperfine transitions [19] [Fig. 4.1(c)] and produces one combined resonance for each $|m_s = 0\rangle \leftrightarrow |m_s = \pm 1\rangle$ transition [Fig. 4.1(e)]. Samarium cobalt ring magnets (SuperMagnetMan) are used to apply a 1 mT static external magnetic field along the (111) NV orientation ($\hat{z}_{\mathrm{NV}}$). More details about the experimental setup can be found in the Supplemental Material.

We first use the magPI platform to image the static dipolar magnetic field produced by a 50 nm dextran coated $CoFe_2O_4$ ferromagnetic nanoparticle (micromod Partikeltechnologie) deposited and dried onto the diamond sensor surface [Fig. 1(b)]. These bio-compatible particles produce nano-scale magnetic fields which lie in the dynamic range of the NV sensing ensemble defined by $\delta\nu$ of the resonance curves. For other imaging applications, the sensor dynamic range can be increased at the expense of magnetic sensitivity by RF broadening the resonance curve.

We then demonstrate dynamic magnetic imaging using the DDQ technique on a tethered-particle-motion (TPM) assay [31]. 500 nm streptavidin coated ferromagnetic nanoparticles (micromod Partikeltechnologie 05-19-502) were tethered by 940 bp single DNA molecules to the diamond surface. The diamond-DNA-particle tethering protocol follows Ref. [45]. Fluid flowed through the sample chamber alters the orientation of the nanoparticle magnetic moment, and the changing magnetic field is imaged at a high frame-rate.

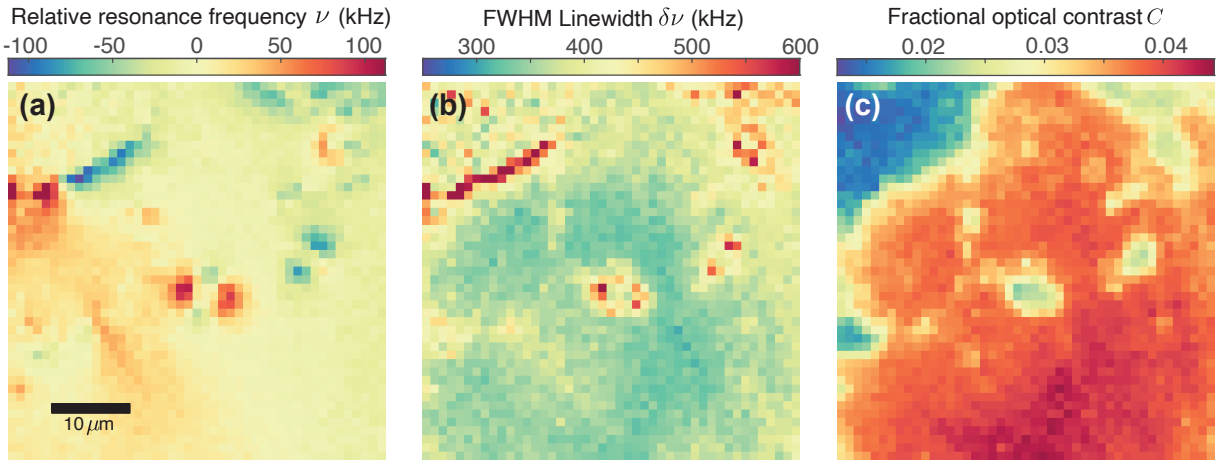

Figure 4.2: Multiple mechanisms lead to changes in NV ODMR on a micron scale when imaging static magnetic dipole and strain fields. (a) Resonance frequency ν shifts due to magnetic field and crystal strain. (b) The FWHM linewidth $\delta\nu$ varies due to gradients of magnetic and strain fields that inhomogenously broaden the NV ODMR in each pixel. (c) Optical contrast C also varies due to due to inhomogenous broadening of the NV ODMR.

4.3 Static Magnetic Imaging Modality

To measure static fields, the full NV resonance curve can be measured in wide-field with arbitrarily long acquisition times. Taking a series of PL images over a range of RFs allows fitting of the entire resonance

response in the measured range. Mapping the fitted resonance frequency at each pixel results in a partial reconstruction of the magnetic field as seen in Fig. 4.2(a). Taking the difference between the $|m_s = 0\rangle \leftrightarrow |m_s = \pm 1\rangle$ resonance frequency maps eliminates shifts of the resonance due to fields other than the magnetic field, and enables imaging of the absolute magnetic field projection along the NV symmetry axis [27], as seen in Fig. 4.3(a).

For quickly-varying magnetic fields, imaging via the static magnetic imaging procedure may not be possible. We thus require a dynamic imaging modality that reproduces the absolute magnetic field across the imaging field of view without prior per-pixel calibration and is compatible with high-frame-rate imaging.

Dynamic Magnetic Imaging Modalities

Single Quantum Difference Imaging

The simplest dynamic imaging modality uses RF excitation applied at one inflection point of one of the NV resonance curves [Fig. 4.1(e)]. PL images taken with RF π-pulses applied are subtracted from PL images taken without RF to detect changes in emitted NV PL [95]. We define a SQ difference image (DI) as

$$\mathrm{SQ}(f_1) = \frac{I_{\mathrm{off}} - I_{\mathrm{on}}(f_1)}{I_{\mathrm{off}}}, \tag{4.2}$$

in which $I_{\mathrm{on}}(f_1)$ is the intensity image taken with applied RF π-pulses at f_1 and I_{off} is the image taken with no applied RF. We assume the NV ensemble is operating in the linear-response regime of the resonance curve, i.e. $\gamma_{\mathrm{NV}}\hat{z}_{\mathrm{NV}} \cdot \vec{B} < \delta\nu$. The per-pixel signal is then given by

$$\mathrm{SQ}^{\mathrm{pp}}(f_1) = \frac{9}{8}C - \frac{3\sqrt{3}}{4}\frac{C}{\delta\nu}(\nu(\vec{E}, \vec{B}, T, ...) - f_1). \tag{4.3}$$

As discussed above, the resonance frequency ν depends on the magnetic field $\vec{B}$ and also varies with local electric field $\vec{E}$, temperature T, and crystal strain.

Additionally, variations in curve-shape, and thus C [Fig. 4.2(b)] and $\delta\nu$ [Fig. 4.2(c)], cause variations of the resonance curve inflection point, contributing to the SQ signal. Microscopic and mesoscopic strain inhomogeneities result in inhomogeneous broadening of the resonance curve [43]. Also, dephasing due

to dipolar interactions between sensing NV centers and other paramagnetic impurities (e.g. P1 and NV) fundamentally limit the NV ensemble coherence, and thus, ODMR linewidth [44; 9].

The SQ DI enables imaging of some nano-scale magnetic structure, but the sensitivity of this technique is limited. In Fig. 4.3(b) we show a SQ DI image with its corresponding static magnetic field map in 4.3(a). The SQ DI enables partial mapping of the magnetic field projection, but is limited by contributions to the resonance frequency shift by strain gradients, as seen in the SQ-signal-color-gradient from upper-left to lower-right in Fig. 4.3(b).

4.3.1 Double Quantum Difference Imaging

Temperature, electric field, and strain shift the zero-field-splitting of the NV ground state, causing common-mode shifts of the $|m_s = 0\rangle \leftrightarrow |m_s = \pm 1\rangle$ transitions [48]. Conversely, the magnetic-field-induced Zeeman effect splits the two transitions. Thus, by probing the difference of the two transition resonance frequencies, the common-mode shifts can be subtracted out and the magnetic field projection can be measured directly. We use a DQ driving scheme [26; 62], applying two-tone RF π-pulses at the opposite inflection points of the two resonance curves simultaneously [Fig. 4.1(e)]. We construct a DQ DI by subtracting the PL image taken with DQ RF driving from an image taken with no RF applied

$$\mathrm{DQ}(f_1, f_4) = \frac{I_{\mathrm{off}} - I_{\mathrm{on}}(f_1, f_4)}{I_{\mathrm{off}}}, \tag{4.4}$$

in which $I_{\mathrm{on}}(f_1, f_4)$ is the image taken with applied RF π-pulses at f_1 and f_4 simultaneously, and I_{off} is the image taken with no applied RF. We again assume linear-response of the resonance curves and additionally assume that the two resonance curves have the same shape (see Supplemental Material). The per-pixel DQ signal is

$$\mathrm{DQ}^{\mathrm{pp}}(f_1, f_4) \approx \frac{9}{4}C - \frac{3\sqrt{3}}{4}\frac{C}{\delta\nu}(f_1 - f_4) - \frac{3\sqrt{3}}{4}\frac{C}{\delta\nu}(2\gamma_{\mathrm{NV}}\hat{z}_{\mathrm{NV}} \cdot \vec{B}). \tag{4.5}$$

By defining $\langle\vec{B}\rangle$ as the average magnetic field over the imaging field of view, Eq. 4.5 simplifies to

$$\mathrm{DQ}^{\mathrm{pp}}(f_1, f_4) = \frac{9}{4}C + \frac{3\sqrt{3}}{4}\frac{C}{\delta\nu}2\delta_0 - \frac{3\sqrt{3}}{4}\frac{C}{\delta\nu}\left(2\gamma_{\mathrm{NV}}\hat{z}_{\mathrm{NV}} \cdot \left(\vec{B} - \langle\vec{B}\rangle\right)\right), \tag{4.6}$$

where $2\delta_0 = (f_4 - f_1) - 2\gamma_{\text{NV}}\hat{z}_{\text{NV}} \cdot \langle\vec{B}\rangle$. By applying f_1 and f_4 at the outer inflection points of the NV resonance curves simultaneously [Fig. 4.1(e)], intensity changes induced by non-magnetic, common-mode shifts are cancelled out, while splittings caused by magnetic signal result in a sum of changes in PL intensity. Hence, for constant C and $\delta\nu$, the DQ DI technique enables absolute magnetic imaging. [26]

Although the contribution of strain-induced-resonance-shifts to the imaging have been eliminated, overcoming the sensitivity limits of the SQ DI, we demonstrate that DQ DI has *increased* the effect of variations in curve-shape on the magnetic imaging. More specifically, variations of C and $\delta\nu$ still cause perturbations of the first two terms in Eq. 4.6. This effect can be seen by comparing the map of C in Fig. 4.2(c) to the DQ DI in Fig. 4.3(c). Thus, for practical applications of the DQ method to wide-field imaging, we find that curve-shape variations dominate and the DQ DI (Fig. 4.3(c)) is ineffective at reproducing a map of the magnetic field projection (Fig. 4.3(a)).

4.3.2 Double-Double Quantum Difference Imaging

To suppress the imaging dependence on curve-shape, we apply bias RFs on either side of the resonance curves [35]. We construct a DDQ DI

$$\text{DDQ} = 2\frac{I_{\text{on}}(f_1, f_4) - I_{\text{on}}(f_2, f_3)}{I_{\text{on}}(f_1, f_4) + I_{\text{on}}(f_2, f_3)} \tag{4.7}$$

where $I_{\text{on}}(f_1, f_4)$ ($I_{\text{on}}(f_2, f_3)$) is the image taken with RF applied at the outer (inner) inflection points of the two resonance curves simultaneously, as shown in Fig. 4.1(e). By applying DQ bias RFs on either side of the resonance curves, the effects of variations in the shape of the the ODMR curve and external non-magnetic fields are mitigated. Here, the DDQ DI signal is normalized by dividing by the mean of the individual DQ frames $I_{\text{on}}(f_i, f_j)$.

Because of the choice of RF, the per-pixel DDQ signal simplifies in a similar manner as the DQ signal in Eq. 4.6 giving

$$\text{DDQ}^{\text{pp}} \approx \frac{3\sqrt{3}}{2}\frac{C}{\delta\nu}\left(2\gamma_{\text{NV}}\hat{z}_{\text{NV}} \cdot \left(\vec{B} - \langle\vec{B}\rangle\right)\right). \tag{4.8}$$

DDQ eliminates the first two terms of the DQ DI signal Eq. 4.6 to obtain a single term which is linearly proportional to $(\vec{B} - \langle\vec{B}\rangle)$. There is still multiplicative dependence on C and $\delta\nu$, but because the shift of the resonance frequency far (> 1 μm) from magnetic field sources falls off faster than the impact of spatial variations of curve-shape due to inhomogeneous broadening, there is no DDQ signal generated in regions with no magnetic field. The DDQ DI completely eliminates the large-scale, non-magnetic gradients in the SQ DI [Fig. 4.3(b)] and suppresses the C and $\delta\nu$ dependence [Fig. 4.2(b-c)] of the DQ DI [Fig. 4.3(c)]. As shown in Fig. 4.3(d), DDQ DI provides similar magnetic sensitivity as the static magnetic projection map in Fig. 4.3(a), with a greater than four-fold acquisition-time-reduction. The static imaging modality requires enough images to fit both resonance curves; the DDQ modality instead extracts the magnetic field dependence of the resonances with only two images: $I_{\text{on}}(f_1, f_4)$ and $I_{\text{on}}(f_2, f_3)$. While the integration time of the DDQ image shown in Fig. 4.3(d) was chosen to match the signal-to-noise ratio of the magnetic field map in Fig. 4.3(a), DDQ enables even faster magnetic imaging as demonstrated in the next section.

We emphasize the general conditions for applicability for the DDQ method: (i) the resonance curve shapes of the two NV spin transitions used must be matched by driving each transition with equal Rabi frequency, (ii) non-magnetic inhomogeneities across the imaging field of view must be smaller than the resonance FWHM linewidth in order to be suppressed, and (iii) sensor operation is in the linear regime, i.e. magnetic signals to be imaged are smaller than the resonance FWHM linewidth. We discuss errors associated with condition (i) in the Supplemental Material, and note criteria (ii) and (iii) are prerequisites for any intensity-based wide-field magnetic imaging involving NV ensembles.

4.4 Wide-field Dynamic Magnetic Microscopy

To demonstrate that DDQ difference imaging can facilitate high-frame-rate imaging of dynamic fields, we image the changing magnetic field produced by a ferromagnetic nanoparticle tethered to the diamond sensor surface by a single DNA molecule. The approximate diamond-particle distance is 400 nm. Fig. 4.4a shows an 8 s time-averaged image of the field produced by the magnetic nanoparticle. A preferred direction is observed due to the partial alignment of the ferromagnetic nanoparticle moment orientation to the 0.35 mT external magnetic-field, oriented along (θ, ϕ)=(54.735°,0°). Next, phosphate-buffered-saline is pulled from a reservoir through the sample channel by a syringe pump at 4 ml/min. The fluid flow exerts a hy-

drodynamic force and torque on the tethered-particle, causing it to reorient, changing the magnetic field at the diamond sensor surface. Fig. 4.4b displays characteristic frames, in chronological order, showing time-resolved imaging of the nanoparticle moment reorientation at a 15.6 Hz frame-rate (64 ms per frame), with insets showing fitted DDQ images displaying the changing magnetic-moment direction in each frame. The fluid-flow-steady-state nanoparticle orientation is imaged with an 8 s time-averaged DDQ image in Fig. 4.4c. The full dynamic magnetic imaging video and simulation information can be found in the Supplemental Material. This experiment represents the novel application of micron-scale dynamic magnetometry to a single-molecule biological system.

Conclusion and Outlook

Although the NV community has made significant progress toward eliminating inhomogeneities in NV ensemble-based-sensors through advanced NV fabrication [2], quantum control methods can significantly increase the sensitivity of these systems for magnetometry applications [9]. However, existing wide-field schemes fail to reliably image magnetic fields due to micron-scale variation in the resonance-curve shape. Here, we introduce a novel quantum control technique, double-double quantum difference imaging, that is suitable for mitigating inhomogeneities in wide-field dc magnetometry to enable imaging of time-varying fields. Using four-tone RF pulses and only a two-image sequence, we show both theoretically and experimentally that DDQ difference imaging not only mitigates non-magnetic perturbations of the NV resonance frequency but also variations of resonance curve-shape. Static-field imaging reveals that these resonance shape variations can be the dominant source of imaging noise in a state-of-the-art NV magnetic imaging surface. Finally, we use the DDQ technique to perform wide-field magnetic microscopy of a dynamic, biological system, enabling high frame-rate orientation imaging of a magnetic nanoparticle tethered to the diamond sensor by a single DNA molecule. DDQ difference imaging eliminates the need for per-pixel calibration and enables high-frame-rate magnetic microscopy via NV photoluminescence intensity imaging.

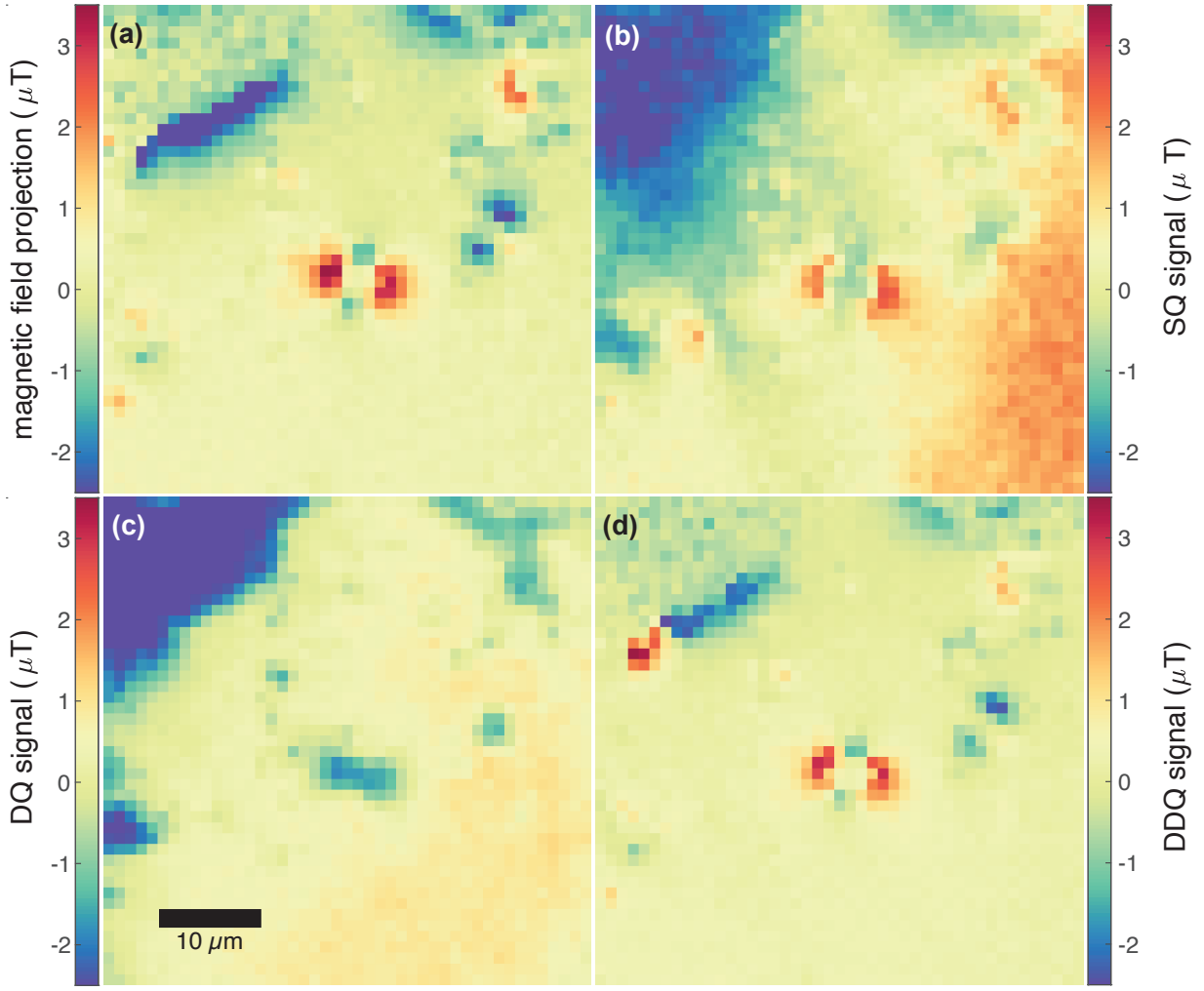

Figure 4.3: Competing magnetic imaging modalities. (a) 'True' static magnetic field projection map generated with the frequency scanning technique outlined in the above Static Magnetic Imaging Modality section (acquisition time 12 s). (b) Single quantum difference imaging (2.4 s). The signal measured with the SQ DI modality is a convolution of the magnetic and strain fields, which are impossible to separate with a single measurement. (c) Double quantum difference imaging (2.4 s). While the DQ DI modality has reduced the impact from the fields that homogeneously shift the NV centers, the DQ signal is more sensitive to the local contrast and linewidth variations of the NV sensing curves. (d) Double-double quantum difference imaging (2.4 s). An inspection of the competing dynamic imaging schemes (b-d) reveals that both the SQ (b) and DQ (c) schemes are significantly compromised by spurious contrast caused by strain gradients and curve-shape variation, respectively, while the DDQ scheme (d) faithfully approximates the 'true' magnetic field projection (a) with a decreased acquisition time.

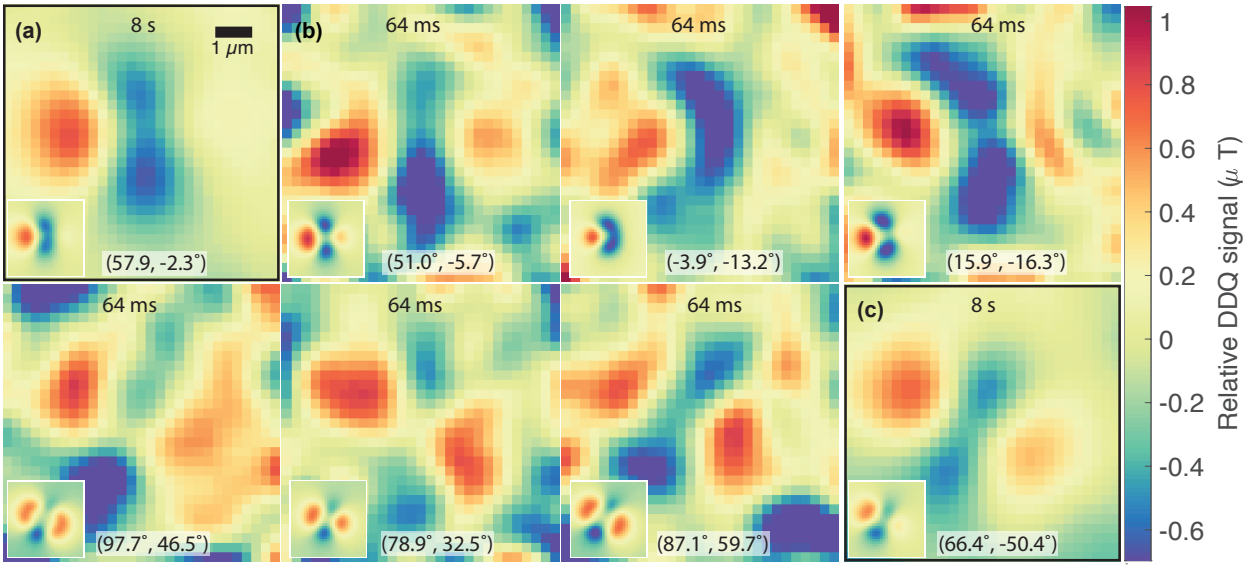

Figure 4.4: DDQ imaging of the reorientation of a DNA-tethered magnetic nanoparticle under applied flow. In each panel, the observed DDQ image is compared with a fitted DDQ image (inset) to estimate the magnetic nanoparticle dipole orientation (θ, ϕ), where the NV ensemble symmetry axis is (54.735°, 0°). For all DDQ DI in this figure, a Gaussian smoothing filter with $\sigma = 533$ nm is applied. (a) A time-averaged DDQ DI (8 s) showing initial magnetic nanoparticle orientation before flow. (b) Representative DDQ frames (64 ms of exposure) showing nanoparticle reorientation in response to an applied flow. (c) A time-averaged DDQ DI (8 s) showing the final magnetic nanoparticle orientation with applied flow.

Chapter 5

Development of single molecule DNA magnetic micro-torque balance

5.1 Introduction

In this chapter, work towards developing a single molecule torque balance experiment is presented. A portion of this chapter is a preprint for a paper connected to results from this work.

5.2 Magnetic micro-torque Balance Experimental Design

In the micro-torsional balance, the orientation of the DNA molecule will be measured and manipulated using a ferromagnetic nanoparticle. The nanoparticle orientation will be measured using a recently-developed quantum-magnetic-imaging modality, MagPI, in which the magnetic field is quantitatively imaged at a sub-micron scale.

A torsional balance is an experimental apparatus that applies a torque to directly characterize bending or twisting (as opposed to stretching) of an elastic object. The macroscopic versions of these apparati are used in many interesting and contemporary applications in the context of physics and engineering [36]. In the current context, this approach aims to directly measure torsional elastic response of a single DNA molecule to bending. The primary goal is to measure the bend angle as a function of applied torque. Sequential

measurements will generate a *torque-bend curve*.

There are already a number of single-molecule characterizations of DNA mechanics which are similar in spirit to this approach: The most well known is the force-extension measurement, which was discussed in the 3 [13]. A second and more natural precedent is the rotor-bead experiment of Bryant, Gore, *et al* where the mechanical response of DNA to twist was characterized [12]. In exact analogy to what was proposed in the LSEC model, the mechanical response to large twist angles was linear and not quadratic as predicted by an elastic model [93].

In most previous experiments, the properties of DNA molecules longer than a persistence length were probed. What is novel about this experiment is that it mechanically manipulates DNA molecules that are *more than 100-fold shorter* than those probed in force-extension experiments. These short-contour-length experiments are essential to probe the tight-bending regime [91] and these short-contour-length measurements can be used to directly generate effective models of DNA conformational statistics in the biologically-relevant tight-bending regime.

In addition to facilitating a new generation of DNA mechanics experiments, this approach will be widely applicable to other single-molecule biophysical systems. An important feature of this approach is that the probe is unbleachable and is therefore applicable to a wide range of systems where a long duration of observations and/or a high frame rate are desirable.

5.3 Proof of Principle Measurement - Unconstrained Bead-DNA Attachment

To generate a baseline measurement and verify the magnetic-torque balance approach, a control with unconstrained Bead-DNA attachment is conducted first. Beginning with this simplified model does not give new information about DNA mechanics, but has two important outcomes: 1) testing and debug-ing sample prep techniques 2) demonstrating that that the imaging techniques and analysis pipeline are able to capture expected results. [1]

Due to the ball-in-socket nature of the biotin-streptavidin interaction, DNA constructs that rely on a

[1] Some text in this section came from a proposal created by :
Paul A. Wiggins, Kai-Mei C. Fu, Zeeshawn Kazi, and Isaac Shelby

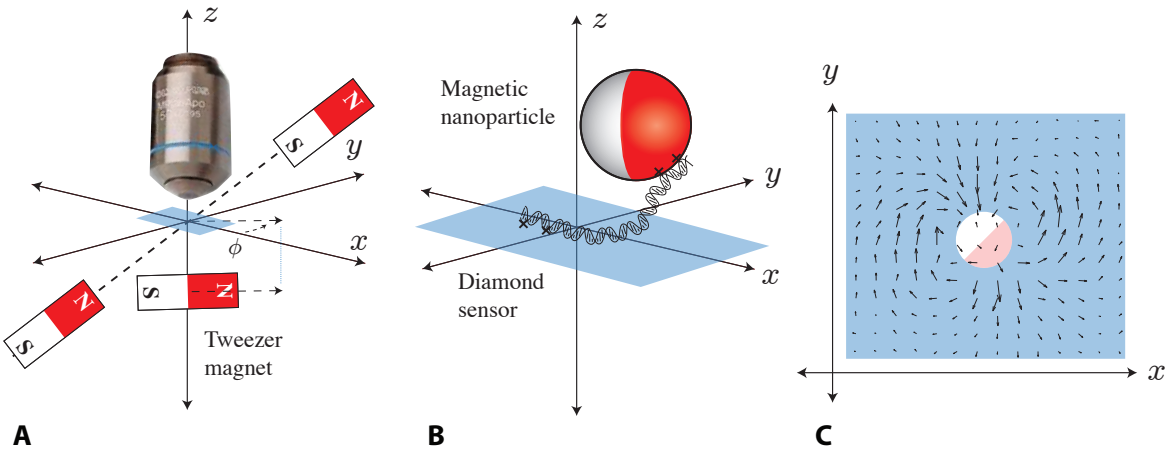

Figure 5.1: Panel A: Next-generation magnetic tweezer. A low-magnitude symmetry-breaking magnetic field is applied at all times. A second tweezer field is used to manipulate the sample. Both the magnitude and direction of the tweezer field are manipulable. **Panel B: DNA-tethered nanoparticles.** Magnetic nanoparticles are functionalized to bind specifically to bio-molecules. **Panel C: Imaging the magnetic field.** A 3-component dipole magnetic field generated by a magnetic nanoparticle is measured at the diamond sensor using the MagPI imaging modality. The plot shows the x and y components of measured magnetic field generated by a nanoparticle.

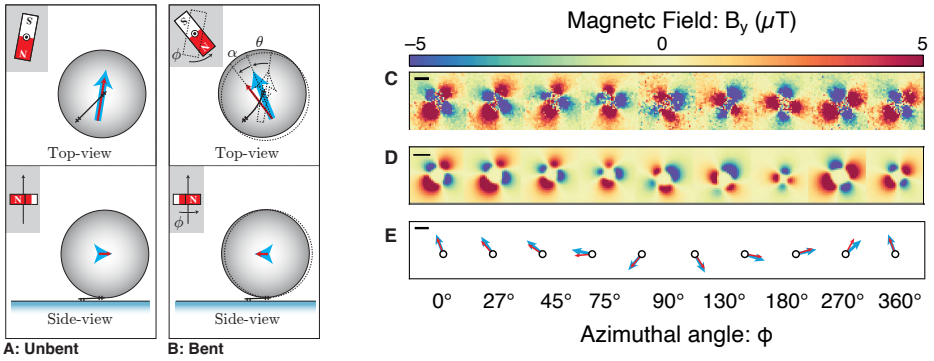

Figure 5.2: Panel A: The micro-torsional balance. A short-contour-length DNA molecule is tethered at one end to the surface and at the other to a ferromagnetic nanoparticle. Panel A shows an unbent molecule with the bead moment and magnetic field aligned. **Panel B:** The magnetic tweezer is then rotated to generate a torque. The DNA molecule bends to deflection angle θ, where torque balance is achieved and the magnetic and bending torques are equal. **Panel C: Rotation series.** A 2-μm ferromagnetic nanoparticle is tethered by a 100-bp DNA molecule using torsionally-free chemistry. The tweezer magnet is then swept through a 360° rotation and a series of MagPI images were collected. **Panel D: Fit to rotation series.** To determine the orientation of the magnetic nanoparticle, the dipole field is fit to a quantitative image model to infer the moment orientation and the external field orientation. **Panel E: Measured dipole and field orientations.** The inferred dipole moment and field orientations are shown.

single biotin modification on the end of the molecule are bound with rotational freedom. This means that when rotating the applied magnetic field tweezer, the DNA will be unable to apply a torque to the attached bead and the magnetic moment of the bead will track directly with the applied magnetic field.

These results can be seen in 5.5 and 5.4.

Seeing direct tracking of the applied magnetic field with the bead mangetic moment verifies several aspects of our experimental design and analysis. This confirms that the generation of DNA-bead complexes specifically bound to the surface of the magnetic-field-sensing chip. Additionally, this confirms the ability to make measurements of the magnetic field of a magnetic nano-particle before damaging the chip surface-DNA-bead complexes and (and can quantify) the accuracy and precision of our bead magnetic particle parameter fitting.

Developing the micro-torsional balance

A torsional balance is an experimental apparatus that applies a torque to directly characterize bending or twisting (as opposed to stretching) of an elastic object. The macroscopic versions of these apparati are used in many interesting and contemporary applications in the context of physics and engineering [36]. In the current context, we are proposing to directly measure torsional elastic response of a single DNA molecule to bending. The primary goal is to measure the bend angle as a function of applied torque. Sequential measurements will generate a *torque-bend curve*.

There are already a number of single-molecule characterizations of DNA mechanics which are similar in spirit to that we are proposing: The most well known is the force-extension measurement, which we have already discussed in the introduction [13]. A second and more natural precedent is the rotor-bead experiment of Bryant, Gore, *et al* where the mechanical response of DNA to twist was characterized [12]. In exact analogy to what was proposed in the LSEC model, the mechanical response to large twist angles was linear and not quadratic as predicted by an elastic model [93].

In most previous experiments, the properties of DNA molecules longer than a persistence length were probed. What is novel about our proposed experiment is that it mechanically manipulates DNA molecules that are *more than 100-fold shorter* than those probed in force-extension experiments. These short-contour-length experiments are essential to probe the tight-bending regime [91] and these short-contour-length

measurements can be used to directly generate effective models of DNA conformational statistics in the biologically-relevant tight-bending regime.

In addition to facilitating a new generation of DNA mechanics experiments, we expect this approach will be widely applicable to other single-molecule biophysical systems. An important feature of this approach is that the probe is unbleachable and is therefore applicable to a wide range of systems where a long duration of observations and/or a high frame rate are desirable.

Assemble a DNA-tethered-particle micro-torsional balance

DNA is bent in the x-y plane of the diamond sensor by applying a torque (in the z direction) to a ferromagnetic nanoparticle. See the experimental schematic in Fig. 5.2. In short: DNA molecules are first tethered to the diamond surface and then to ferromagnetic nanoparticles using either torsionally-free binding chemistry [29] or torsionally-constrained binding chemistry [12]. The nanoparticles are then rotated by the magnetic-tweezer field, and, in the case of the torsionally-constrained binding chemistry, the DNA molecules are bent.

Both torsionally-free and torsionally-constrained DNA tethers with ferromagnetic nanoparticles using 2-μm ferromagnetic Spherotech particles as well as 50-nm Turbobeads have been constructed. By analyzing the tethered-particle-motion in bright-field or dark-field imaging, the motion of the torsionally-free particles generated the expected rotationally symmetric distribution of nanoparticles positions while the torsionally-constrained particles generated the expected parenthesis-shaped distribution of nanoparticle positions. In both protocols, some subset of the nanoparticles are stuck. These samples are then imaged these samples on the MagPI microscope [40]. As expected, dipole-like field patterns are only observed when magnetic particles are present. (iii) In the *strong-tweezer-field limit*, the magnetic moments align with the applied magnetic field as expected while some, consistent with stuck beads, remain unaligned with the magnetic field. (iv) As the tweezer magnet rotates the external magnetic field and the aligned beads rotate with the magnetic field and remain aligned, as expected. See Fig. 5.2A-E.

For a micro-torsional balance, the key observable is the *angular deflection* (i.e. angular orientation of the probe) at a sequence of applied torques generated by the magnetic tweezer. In the micro-torsional balance, the probe orientation, position and magnetic moment are inferred by the local magnetic fields they

generate, which are imaged using MagPI. These observed images are then fit to a quantitative image model to determine the orientation, position and magnetic moment. The generation of these image models is therefore a key step in measuring angular deflection.

The detailed physical model for describing the photoluminescence is already well-known [40]. The challenge in this is to adapt this known model to computationally predict pixel intensities as a function of probe orientation, position and magnetic moment. The detailed model is parameterized by a three dimensional bead position, a two-dimensional bead-moment orientation and a magnetic-dipole-moment magnitude. The angular deflection is measured by fitting the model images to the experimental data. A statistical model is required to estimate the uncertainties in the model parameters from the image fit. We model the pixel intensities as Gaussian random variables with fixed variance and a mean predicted by the model described above. We then use a least-squares minimization to optimize the parameter values and the uncertainties are estimated from the Jacobian.

Introduction

Despite the long history of research into DNA's bio-mechanical properties [85], the energy requirements of bending short, 75-300 base pair (bp) DNA molecules has not been fully understood. DNA flexibility is relevant for transcription regulation [30; 34] and chromosomal packaging [92; 22; 78]. Long (compared to histone scales) DNA length measurements point to a polymer bend energy model that is quadratic in bend angle called the worm-like-chain (WLC) model with length-independent persistence length of 150 base pair (bp) [92]. However, cyclization measurements at length scales shorter than the persistence length demonstrate that bends are significantly more probable than the WLC model predicts [87; 22]. The lack of study of the bend response of short DNA molecules is in part due the difficulty of measuring torque exerted by individual DNA molecules and the challenge of probing the bend response at the short length scales. [2]

[2]This section and the remainder of this chapter is an as yet unpublished preprint, expected authorship: Zeeshawn Kazi, Isaac M. Shelby, Ruhee Nirodi, Joseph Turnbull, Paul A. Wiggins, Kai-Mei C. Fu.

5.4 Nano-mechanical torque balance

In this work, a nano-mechanical torque balance is used to measure the bend response of individual DNA molecules (Fig. 5.3A). A DNA molecule is attached at one end to a diamond quantum magnetic field sensor and at the other end to a ferromagnetic nanoparticle probe. The orientation of the magnetic probe and applied field are measured using quantum magnetic imaging of an near-surface ensemble of nitrogen-vacancy defects in the diamond sensor [41]. The DNA molecules are bent through multiple angles using a magnetic tweezer field. The probe moment direction $\vec{m}$ and the applied magnetic field $\vec{B}$ are measured simultaneously, and the torque exerted by the DNA as a function of bend angle is measured by imaging deflections between the applied field and the nanoparticle moment vectors.

5.5 Probe orientation measured by quantum magnetic field imaging

Wide-field quantum vector magnetometry using a near-surface ensemble of nitrogen-vacancy defects in diamond is performed to measure the dipole orientation of the ferromagnetic nanoparticle probes attached to the DNA molecules [49]. Two optical resonances for each of four NV crystallographic orientations are measured across an imaging field of view (Fig. 5.3B). The microtesla-scale probe magnetic field superposes with the millitesla-scale applied field. This mismatch in scales allows for simultaneous measurement of both probe and applied magnetic fields. The measured probe fields (Fig. 5.3C) are fit by a least-squares method to a six-parameter magnetic dipole model that comprises the probe position and magnetic moment vectors (Fig. 5.3D). The residual between measured and fit images is shown in Fig. 5.3E.

5.6 Dipole orientation illuminates distinct DNA binding configurations

To demonstrate the ability of the nano-mechanical torque balance to probe DNA bending, ferromagnetic probes were used in three distinct bio-mechanical constructs. In the first case, the probe was tethered by a torsionally-free DNA tether in which the probe-DNA and DNA-surface attachments are each accomplished by a single binding site. The torsionally-free DNA tethered magnetic probe is free to align to the applied field (Fig. 5.4A). This control experiment demonstrates the ability of the diamond platform to effectively measure dipole orientation and validates the diamond-DNA tethering protocol. In the second configuration,

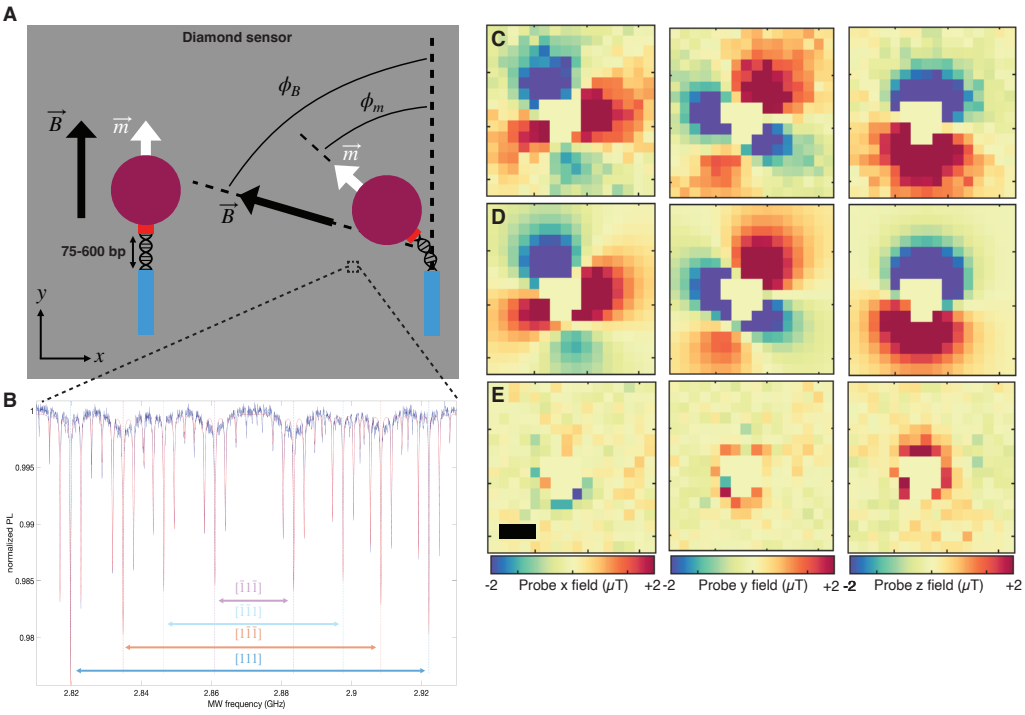

Figure 5.3: Nano-mechanical torque balance. (**A**) Diagram of experiment showing top-down view of a single DNA molecule attached at one end to a diamond sensor and to a magnetic nanoparticle probe at the other end. An applied magnetic field reorients the probe magnetic moment. The torque exerted by the applied magnetic field on the probe is balanced by the bending torque exerted by the DNA on the probe. (**B**) Optically-detected-magnetic-resonance (ODMR) of four NV crystallographic orientations is measured across the imaging field of view. The ODMR spectrum contains information about both the applied magnetic field and the probe magnetic field. (**C**) Measured probe magnetic field vector projections, (**D**) fit probe magnetic field projections and (**E**) residuals between measurement and fit. Scale bar is 2 μm.

the magnetic probe is immobilized on the diamond sensor surface in the absence of DNA so the probe magnetic moment is fixed by the surface interaction, no matter the direction of the applied field (Fig. 5.4B). In the torque-balance configuration, the ferromagnetic probe is tethered by 600 bp DNA molecules with multiple binding sites at the probe-DNA and DNA-surface interfaces so that both the applied field and DNA are able to exert a torque on the ferromagnetic probe (Fig. 5.4C).

These three distinct bio-mechanical configurations result in qualitatively different magnetic dipole orientations with respect to changing applied field direction. In Fig. 5.4A, the dipole moment projection along the magnetic moment vector is shown for a torsionally-free DNA tether. The dipole moment points along the applied field direction. In Fig. 5.4B the particle immobilized on the diamond sensor surface is seen to maintain its orientation no matter the direction of the applied field. In general, distinct stuck magnetic particles are oriented randomly and maintain their orientation in changing applied field directions.

After these two control experiments, a probe in a nano-mechanical torque balance is examined. The probe dipole moment direction is given by a balance between a torque exerted by the applied field and a torque exerted by the DNA. In Fig. 5.4C, the particle is seen to align with the field for certain angles of the magnetic field and deviates from the applied field from other angles due to the torque applied by the DNA.

5.7 Bend stiffness measurement

To quantitatively measure bend stiffness, the applied field is reoriented and the magnetic particle moment vector is imaged in the torque balance configuration. The applied field direction is reoriented through several revolutions and a nutation of probe magnetic moment about a “home” orientation is observed. The amplitude of this nutation is given by the ratio of the magnetic torque to the DNA torque. A model of probe moment direction as a function of applied field direction is developed and overlaid on the experimental data. For the 600 bp DNA molecules, several experiments are conducted with varying probe magnetic moment magnitudes. In each experiment, the DNA bend response is consistent with the WLC chain model with persistence length of 150 bp. For the 75 bp DNA molecule experiments, the DNA bend response is consistent with the WLC chain model with persistence length of 50 bp.

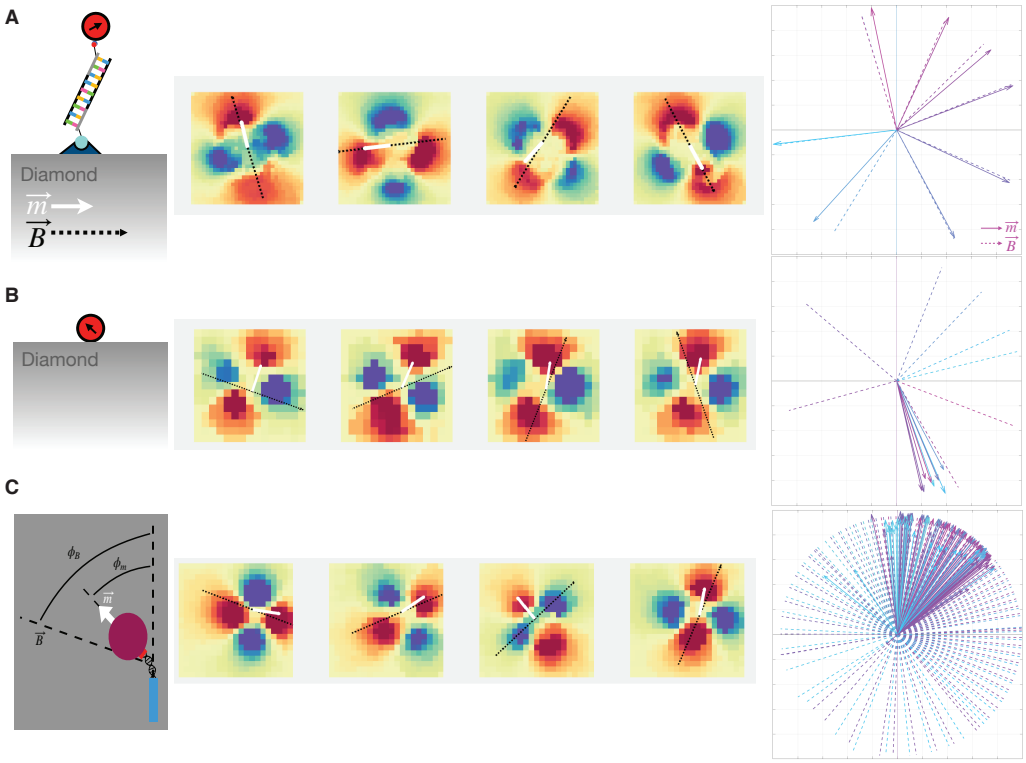

Figure 5.4: Dipole orientation illuminates qualitative differences in DNA binding character, image comparison. Ferromagnetic probe field images with changing applied field angle are shown for three different biomechanical configurations in the three rows, and different applied field directions in the different columns. In each series, the dipole image is shown, overlaid with the fitted moment direction vector in white and the applied field direction vector in dashed black. (**A**) Particle tethered by an free DNA tether. The dipole moment is free to re-orient and points along the applied field direction. (**B**) Particle stuck to the diamond sensor surface. The dipole moment direction is independent of applied field angle and points in a constant direction. (**C**) Probe in a nano-mechanical torque balance. The probe moment direction is balanced by a torque from the applied field and a torque from the DNA. The particle aligns with the field for certain angles of the magnetic field and deviates from the applied field from other angles due to the torque applied by the DNA.

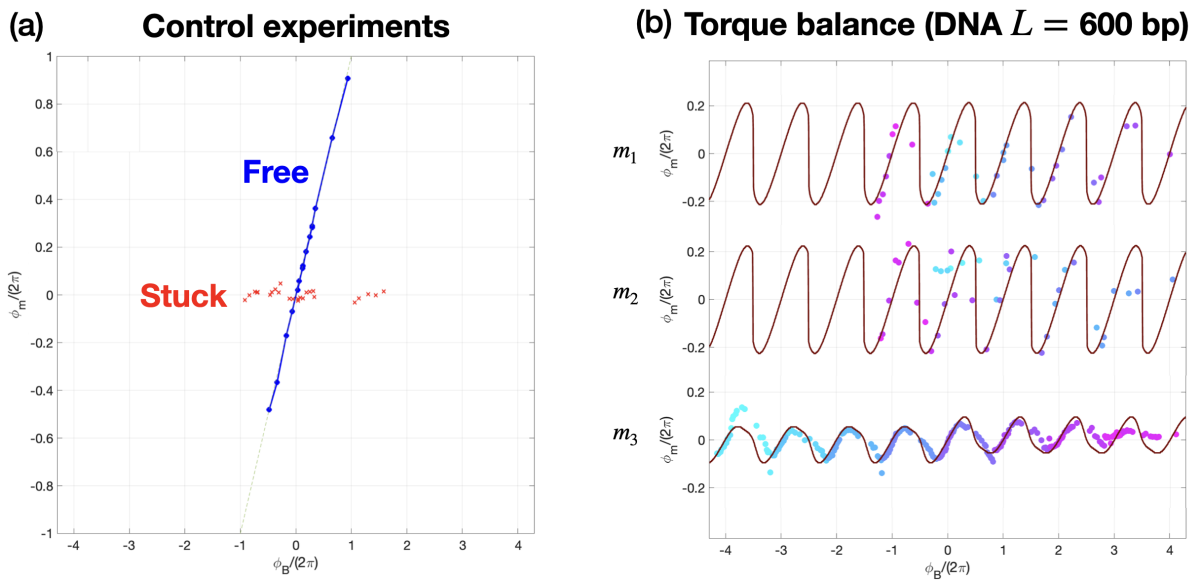

Figure 5.5: Response of dipole to applied field measures bend stiffness. (a) Control experiments: stuck and free particles. The measured magnetic moment in plane angle ϕ_m is plotted as a function of applied field angle ϕ_B . In the stuck case, the dipole direction is constant and independent of applied field direction. In the free case, the dipole direction tracks with applied field. (b) Torque balance response for 600 bp DNA molecules. Three different particles with three different moment magnitudes m_i are shown. The data is consistent with a WLC sinusoidal model with L_p=150 bp.

5.8 Conclusion and Outlook

In this work, a nano-mechanical torque balance is constructed to measure the bend stiffness of individual DNA molecules. A wide-field quantum magnetic particle imaging platform is used to measure the vector magnetic field produced by DNA-tethered ferromagnetic probes in three distinct biomechanical configurations: torsionally-free DNA tether, immobilized magnetic particle and nano-mechanical torque balance. The dipole magnetic field images are fit to measure the dipole moment vector, and the three configurations are distinguished in examining the dipole magnetic moment vector response to the applied field. In the torque balance case, the magnetic moment vector is imaged under a range of applied field directions, and the in-plane magnetic moment angle response is consistent with the WLC model with the nominal value of persistence length. This work demonstrates the viability of the nano-torque balance to measure DNA bend stiffness and opens the door for single-molecule bend stiffness measurements of sub-nucleosome-scale DNA molecules as well as sequence-dependent bending stiffness of individual DNA molecules.

Experimental Methods

An individual single domain cobalt ferromagnetic particle is tethered by a 600 bp DNA molecule in the torque balance configuration. Vector images of the particle magnetic field are fit to a point dipole model with six-parameters, the dipole magnetic moment and position vectors. The three columns show B_x, B_x, and B_z. The first row shows the measured vector images using the PODMR vector magnetometry method. The second row shows the measured images with a gradient mask. The gradient mask is necessary to match the magnetic dipole fit with the experimental data because of the limit of magnetic field gradient observable in the NV platform as mentioned in Chapter 6. The mask is constructed by examining inhomogenous broadening of the NV ODMR and masking pixels with inhomogenous broadening above a cutoff threshold. The third row shows the fitted images using the six-parameter dipole model with the empirically-determined gradient mask. The fourth row shows the dipole model fit without mask. The dipole model predicts high field strengths which produce large magnetic field gradients that are unobservable by the magPI platform, thus the gradient mask is necessary. The fifth row shows the residual between the measured data and the fit with mask, and large residuals appear between the fit and measured data due to the large field gradients

that are not resolved in the experimental data. The sixth row shows the residual between the measured data with mask and the fit with mask. This residual is the most important to minimize as it compares the dipole model and experimental data on equal footing. The magnetic moment vector of the particle is fit and the magnitude of the moment $\approx 5 \times 10^{-18}$ Am^2 is consistent with a prediction for an individual 50 nm cobalt single domain ferromagnetic particle. In this way, fitting magnetic dipole images measures the magnetic moment vector magnitude and direction.

To image the applied magnetic field and the ferromagnetic probe moment, wide-field vector magnetometry is performed as discussed in Chatper 6. Fluorescence images are collected as the applied MW is swept over a range of frequencies, and PODMR of the NV ensemble is recorded. The mean fluorescence count at each MW is fit to a multi-dip Lorentzian. The four Zeeman splittings associated with each NV orientation are then linearly transformed to magnetic field components in the lab frame. Because the magnetic particle dipole field averages to zero over a field of view, the mean ODMR spectrum over an imaging field-of-view measures the applied magnetic field. This mean spectrum fit is used as a guess for each individual pixel's ODMR spectrum. The variations across the imaging field of view are given by the ferromagnetic probe dipole field. In this way, vector magnetometry of the applied magnetic field and probe field vectors is performed simultaneously.

The magnetic particle field components as a function of applied field angle are then fit using least-squares to a six-parameter dipole model as described in Chapter 6. An example of the results of this fitting is show in Figure 5.4.

Chapter 6

Inference in Image Analysis

In the above sections, analysis relied on being able to determine the orientation (and position) of a magnetic dipole generating the 2D field slice we image. The approach is discussed in this section.

6.1 From ODMR to magnetic fields

Once the locations of the resonances in PL intensity have been located, it is relatively straight-forward to determine the magnetic field that lead to those, *if* you know which resonance corresponds to which physical orientation.

As mentioned in Chapter 3, the crystal structure of diamond leads to 4 possible axes the NV +z can lie along. Given a sweep over all 8 of the corresponding ODMR curves (2 for each axis from the NV and "VN" along that axis) there is no information to differentiate them. For known "background" (or splitting) applied field, you can have the splitting field be on a different order of magnitude from the fields that you are attempting to measure. This allows for identification of which of the 4 NV axes each of the 8 central dips belongs to in an emtpy field of view, and relying on the fields that are being measured shifting those slightly from their original positions. There are also techniques that use the polarization of the excitation and collected illumination from the NV centers to differentiate between the NV axes (source). For our magnetic tweezer experiment, we developed an approach for determining the resonance assignment by using knowledge of the form of the applied field.

When the magnetic tweezer lies along an angle that maximally aligns it with the static splitting field, the

resonance order can be determined

Once a resonance assignment is determined, the magnetic field that generated the corresponding ODRM curves can be found by taking a linear combination of the various splittings.

We work in a basis where the [111] axis of the diamond is equally along the x,y, and z axes. This places the x and y axis along the diagonals of a given FOV while the z-axis goes towards the camera.

This gives the unit vectors of the orientations as:

$$\hat{o}_1 = \frac{1}{\sqrt{3}} \langle 1, 1, 1 \rangle \tag{6.1}$$

$$\hat{o}_2 = \frac{1}{\sqrt{3}} \langle -1, -1, 1 \rangle \tag{6.2}$$

$$\hat{o}_3 = \frac{1}{\sqrt{3}} \langle -1, 1, -1 \rangle \tag{6.3}$$

$$\hat{o}_4 = \frac{1}{\sqrt{3}} \langle 1, -1, -1 \rangle \tag{6.4}$$

which gives the magnetic fields as a function of the splittings as

$$\vec{B}_x = \frac{\sqrt{3}}{8} [Z_1 - Z_2 - Z_3 + Z_4] \tag{6.5}$$

$$\vec{B}_y = \frac{\sqrt{3}}{8} [Z_1 - Z_2 + Z_3 - Z_4] \tag{6.6}$$

$$\vec{B}_z = \frac{\sqrt{3}}{8} [Z_1 + Z_2 - Z_3 - Z_4] \tag{6.7}$$

where Z_i is the magnetic field projection along the i orientation. Note that we identify splittings where the magnetic field is parallel to the NV axis as positive and splittings where the magnetic field is anti-parallel to the NV axis as negative.

6.1.1 From Magnetic fields to Dipole Parameters

After the substantial amount of work to optimize PL collection and convert the PL vs RF data to locations of magnetic resonances to local magnetic fields, we come to fitting the dipole moment of the magnetic bead

that generated the measured magnetic field.

Interestingly, the problem of measuring the magnetic field due to a dipole source in a plane has been approached before! Searching for an un-exploded ordinance detection has approached a similar problem. Buried underground either deliberately or from years of buildup, these items are often made with significant ferromangetic materials. The problem of detecting them has been discussed [10]. Unfortunately, the similarities in the two problems ends there, as the scale of that problem is 1000x greater.

We approach the approach the fitting of magnetic bead parameters in the context of a least-squares optimization. As demonstrated above, the Poisson noise with high photon count for each measured PL propagates through to the precision of the magnetic field fitting to make a Gaussian noise approximation of the magnetic field at each pixel appropriate. This is, of course, only for pixels that don't encounter other noise issues.

6.2 Least Squares from Maximum Likelihood Estimate

Begin by treating each pixel in the measured field as an independent measurement with some empirically estimated uncertainty, one can construct a maximum likelihood estimate. Consider the measured magnetic field: $\vec{B}^{ij}$ where superscript indicate the row and column of the pixels in the image. Consider some model that generates a simulated magnetic field $\bar{B}^{ij}(\theta)$ where θ are the model parameters. By modeling each pixel as a Gaussian probability distribution (informed by considering empirically measured distributions of magnetic fields when no source is present) one can express the probability of a set of parameters θ generating the measured field as:

$$P(\vec{B}^{ij}|\theta) = N \prod_{ijk} \exp\left(-\frac{(B_k^{ij} - \bar{B}_k^{ij}(\theta))^2}{2 * \sigma_{ij,k}^2}\right) \tag{6.8}$$

where k indicates the component of the magnetic field, and N is the appropriate normalization prefactor. Converting this a negative loglikelihood provides a method for determining the most likely θ that generated the image observed:

$$-\log q = \sum_{ijk} \frac{(B_k^{ij} - \bar{B}_k^{ij}(\theta))^2}{2 * \sigma_{ij,k}^2} \tag{6.9}$$

minimization of this quantity over possible θ values results in the identification of the most likely θ to generate the magnetic field imaged. There exist a large number of software packages to approach least squares problems with nonlinear functions. In this thesis, the MATLAB function lsqnonlin with the 'Levenberg Marquardt' algorithm was found to be the most resilient to initial guess. All that remains is generating a simulation of the expected field.

For these experiments, the magnetic signal was assumed to always be generated by a magnetic dipole. This works for small single-domain particles, as well as spheres coated in cohesive magnetization. The magnetic field of a dipole was used:

$$\vec{B}(\vec{r}) = \frac{\mu_0}{4\pi}\left(\frac{3(\vec{m}\cdot\vec{r})\vec{r} - \vec{m}r^2}{r^5}\right) \tag{6.10}$$

where $\vec{r}$ is the vector that points from the magnetic dipole to the location of the calculated magnetic field, and $\vec{m}$ is the magnetic moment vector. This was simulated on a lattice of grid points evenly spaced at the expected spacing of NV centers in the sample. Because the NV layer is expected to be shorter than the depth of focus (by design), the magnetic field at each xy point is averaged over the z direction. Then a 2D gaussian filter is applied to the now 2D magnetic field image with a width equivalent to the expected optical resolution of the camera set up. Finally, the xy points are collected into pixels. While in the real experiment the blurring from finite spatial resolution and binning into pixels occurs upstream of the identification of magnetic fields, this necessary computational shortcut was found to be sufficient for well-behaved pixels.

Code for this approach (and the entire analysis pipeline) can be found at: https://github.com/I-Shelby/magPI-bead-fitting. Email imshelby1@gmail.com for access.

6.3 Magnetic field gradient masking

Looking at Figure 6.1 it is very evident that the model of pure dipole field is insufficient to accurately describe the signals detected. This comes from the limiting factor of the imaging process: the pixel size. When collecting light for a single pixel, the detector is collecting emission light from 300 NV centers. Consider the scalar fields that are the local magnetic field dotted into the NV orientations at the location of each NV center. Gradients in this scalar field lead to the resonant frequency of the different NV centers in

the single pixel shifting relative to each other. In cases with a small gradient (quantified later) this leads to a decrease in the contrast and an increase in the linewidth of the ODMR response curve of a pixel. In more extreme cases, the NV centers can be shifted far enough such that the ODMR curve in unable to be resolved above the Poisson noise of the emissions.

To identify pixels that have been impacted by sufficiently large magnetic gradients, it is possible to extract information from the PL counts vs applied RF for each pixel. When a pixel experiences a large magnetic field gradient, the PL intensity varies less over the range of applied RF. Over a field of view, this can be used to differentiate between well-behaved pixels and pixel that are experiencing too large of a magnetic field gradient (and whose measured magnetic field values should be ignored). This is exemplified in Figure 6.2. The exact cutoff for using this will depend on many aspects of the specific data run such as diamond sample, laser intensity, and RF power. As such it is easier to automate this differentiation. We found that for a sufficiently cropped region (no more than 1 um between the edge of the bead signal and the edge of the region) the mathworks package "Linspecer" would successfully differentiate the two families of pixels by generating a colormap for the variance of the PL vs RF curve over the field of view [46]. This is demonstrated in Figure 6.2

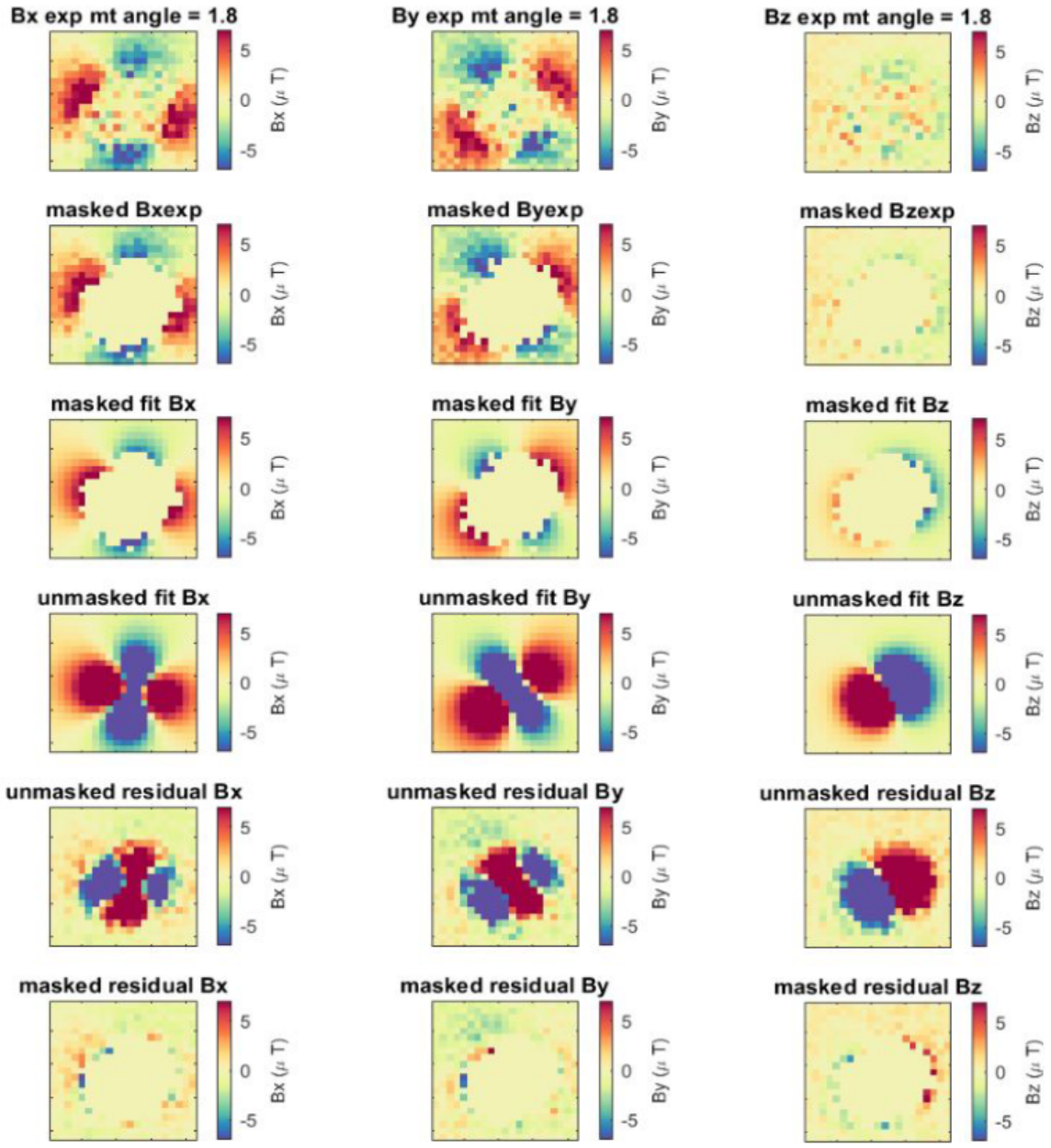

Figure 6.1: Plots of all three components of a measured magnetic field and corresponding least squares fit. Top row: measured magnetic fields. Second row: measured magnetic field after applying gradient mask. Mask determined with method outline in Section 6.3. Third row: simulated magnetic field after applying gradient mask. Fourth row: simulated magnetic field without mask. Fifth row: residual without mask. Sixth row: residual with mask.

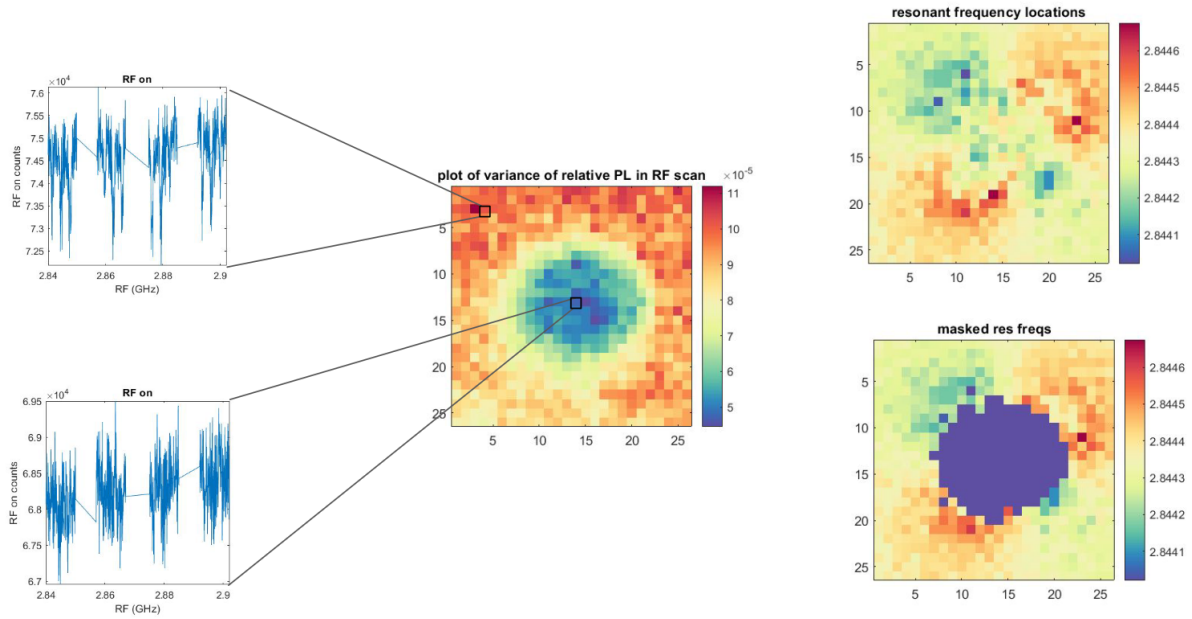

Figure 6.2: Left: Plots of PL counts vs applied RF for pixels with low and high magnetic field gradient. Center: plot of variance of PL counts vs applied RF around a magnetic bead. Right: Plots of detected resonance frequencies with and without pixels masked for having too low variance (corresponding to large magnetic gradient).

Chapter 7

Outlook

This thesis presented development of magnetic imaging techniques for biological assays. It presented both a rapid imaging technique with broad applications to videorate widefield magnetic imaging. It was demonstrated to be able to identify reorientation of a microscale magnetic bead under reorientation from a fluid flow. Additionally, a micro-magnetic torque balance experiment was presented. While further work needs to be done to connect measurements from this set up to significant biophysical breakthroughs, the process of generating data from this technique has been demonstrated.

7.1 Future Applications of DDQ

Less specific than the the micro-torsional balance work presented, DDQ is a simple, widefield, rapid magnetic projecting imaging technique. The most immediate practical application is the potential for real time magnetic imaging of NV samples. Current other real time difference imaging techniques fail to mitigate spatial variation, as discussed in Chapter 4.

For applying DDQ to passive (no active control) biophysical measurements, DDQ will work best moving forward without the need for a static, splitting magnetic field. One method for removing this is Fourier optical processing to separate out the 4 NV crystallographic orientations without splitting with a magnetic field [5]. Once the magnetic interaction is removed, the DDQ technique will be able to give orientation (and position) readouts for biological systems at videorate exposure times.

7.2 Future Applications of micro-torsional DNA balance

This section involves discussing potential future experiments for the torque balance experiment. [1]

The ability of the micro-torsional balance to bend DNA on such short length-scales and be completely free of complicated and subtle assumptions about biochemistry make it the most promising approach to solve the long standing idea that the existing understanding of DNA bending energy fails on short length scales of DNA. The ability of the micro-torsional balance approach to directly measure the bending energy means provides a key parameter to generate quantitative alternative hypotheses.

A second *mechanical language* of DNA sequence is believed to play an important role in many gene-regulatory processes. Any DNA-protein complex in which the DNA-binding protein makes more than one specific contact is dependent on the mechanical properties of the DNA between the specific contacts [98]. Perhaps the most famous example is the DNA roller-coaster loop imagined in the context of Lac-repressor-induced looping between two *lac* operator sites [50]. (See Fig. 3.4A.) Structural differences between the nucleotide bases imply that the mechanical properties of DNA can be sequence dependent and many distinct lines of experimental evidence support this model [33]. Perhaps one of the most elegant examples of this phenomenon is *indirect readout*, the mechanism where the DNA sequence-dependent affinity is purely a consequence of DNA deformation (in regions where there is no protein-DNA contact) [98].

This mechanical language is biologically relevant. Arguably the most biologically important example is nucleosome positioning [33]. (See Fig. 7.1.) The nucleosome consists of roughly a one-and-three-quarter wrapping of DNA (147 bases) around a protein spool, the histone octamer [70]. It forms the lowest-level motif of chromatin structure in the eukaryotic cell. DNA wrapping the histone has lower accessibility relative to DNA in the linker regions between histones and therefore nucleosome positioning plays a central role in transcriptional regulation in eukaryotic cells. What role does DNA deformation play? All DNA sequences bind the histone octamer tightly due to strong Coulomb interactions; however, there is roughly a three order of magnitude variation in the affinity of DNA sequences for histones [84]. A quantitative comparison between histone affinity and the cyclization J factor suggests that this variation in affinity is mechanical in nature [14]. This evidence is extremely important since the typical mechanism for sequence

[1] A version of this section came from a proposal created by :
Paul A. Wiggins, Kai-Mei C. Fu, Zeeshawn Kazi, and Isaac Shelby

specificity is based on a lock-and-key fit between protein and DNA macromolecular structures. However, this does *not* appear to be the case with the nucleosome or else the relative free energies of cyclization and histone affinity would be unrelated. From an evolutionary standpoint, the relative lack of canonical mechanisms of sequence specificity are easy to understand: Histones binds DNA every roughly 180 bp on the eukaryotic genome so they must bind nonspecifically enough to fulfill this role.

The micro-torsional balance has great potential for providing new insight into the sequence dependence of DNA mechanics. It may seem that this approach suffers from some of the same short comings as the J factor approach in that it lacks the ability to interrogate DNA mechanics at the dinucleotide step level (e.g. [65]); however, it does have the ability to apply pure torque, whereas cyclization can be understood to generate a combination of torque and force as a consequence of end-to-end displacement constraints [97], and this property *greatly simplifies* the analysis and interpretation. But a second key advantage of the micro-torsional balance approach is the potential to explicitly probe the role of phasing in the sequence dependence.

The analysis of high-affinity nucleosome sequences reveals that the presence of certain dinucleotide steps is not sufficient and that their positioning is also critical [81; 84]. (See Fig. 7.1.) From a mechanical perspective, the helical structure of DNA is critical and bending into the minor groove appears to be essential to efficient tight bending, at least in the context of nucleosome binding [70; 75; 61]. Resolving the difference in bending relative to the twist of the helix would be extremely difficult in the context of DNA cyclization since the molecule can bend in any direction to form a cycle. In the micro-torsional balance experiments, the sequence of the DNA adaptors which bind the surface and bead can be engineered to control which orientation is bent and therefore this approach can be used to explore this phasing dependence mechanically for the first time.

Another future experiment for the micro-torsional balance could be to detect the predicted asymmetry between minor and major-groove bending. Models for histone affinity predict that bending into the minor groove is more efficient than bending into the major groove. In short: Sequencing of high histone-affinity DNA sequences reveals a phasing relation between dinucleotide steps. AA, TT or TA dinucleotides sequenced appear spaced by the 10-bp helical repeat and GC dinucleotides steps appear 5-bp out of phase with these *soft steps* [84; 75]. The crystal structure of the 601-nucleosome shows that DNA bending is lo-

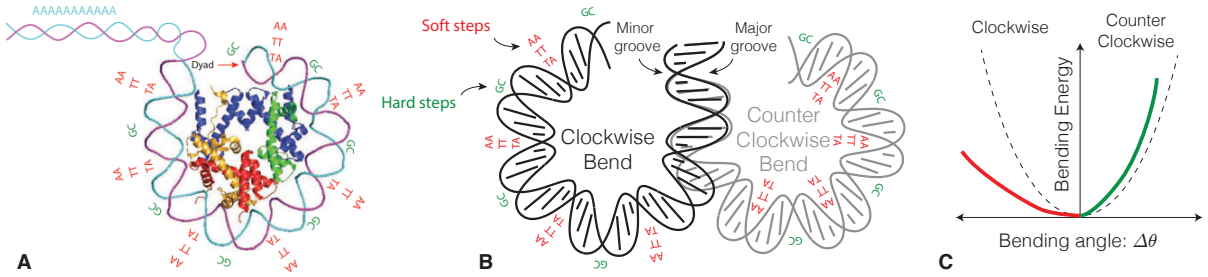

Figure 7.1: Panel A: Nucleosome sequence preferences. There is a preference for dinucleotides steps that occur periodically with the DNA helical repeat and are known to facilitate sharp bending of DNA around the nucleosome. These include ≈10-bp periodic AA, TT or TA dinucleotides that oscillate in phase with each other and localize on the histone so that bending occurs into the minor groove of the helix. These repeats are out of phase with ≈10-bp periodic GC dinucleotides, located where the major groove faces histone. The figure was taken from Ref. [81]. **Panel B: Clockwise bending of a 94mer.** When the 94mer is bent in the clockwise direction, soft base steps bend towards the minor groove. When the 94mer is bent in the counter-clockwise direction, GC base steps bend towards the minor groove. **Panel C: Putative anisotropic bending of DNA.** Bending into the minor groove may be energetically favorable at soft dinucleotide steps.

calized to the AA, TT or TA dinucleotide steps and furthermore occurs into the minor groove of the double helix [70]. Despite the central role that dinucleotide phasing plays in histone affinity and its mechanical interpretation, there has been *no direct test of whether an asymmetry between minor and major-groove bending exists* due to experimental limitations.

The largest stretch goal for the micro-torsional balance is studying sequence-dependent mechanics of DNA. The long term goal of the study of sequence-dependent DNA mechanics is *to construct of quantitative model that can predict the indirect readout or histone affinity as a function of DNA sequence.* The micro-torsional balance *does not* provide the single dinucleotide-step resolution of crystallographic approaches [65; 23; 61]. Although these approaches are *empirical*, *i.e.* they depend on assumptions that cannot be justified rigorously, they do none-the-less seem to generate useful quantitative predictions that match experiment (*e.g.* [61]). It is also important to note that this crystallographic approach has also been extremely powerful in the context of the protein folding problem where the rules learned from observed structures are qualitatively predictive and facilitate the *de novo* design of new proteins.

A promising way forward is to combine these crystallographic-based models as a quantitative hypothesis generation machine and then test them using using DNA mechanics experiments using the micro-torsional balance. Although cyclization is clearly more experimentally tractable, cyclization and histone affinity are probably more suitable methods for model validation. In contrast, the micro-torsional balance proposed here

generates experimental results that directly probe the underlying model and therefore will probably prove a more tractable tool for refining or training the underlying model.

Bibliography

[1] Eisuke Abe and Kento Sasaki. Tutorial: Magnetic resonance with nitrogen-vacancy centers in diamond - Microwave engineering, materials science, and magnetometry. *Journal of Applied Physics*, 123(16), 2018.

[2] V. M. Acosta, E. Bauch, M. P. Ledbetter, C. Santori, K. M.C. Fu, P. E. Barclay, R. G. Beausoleil, H. Linget, J. F. Roch, F. Treussart, S. Chemerisov, W. Gawlik, and D. Budker. Diamonds with a high density of nitrogen-vacancy centers for magnetometry applications. *Physical Review B - Condensed Matter and Materials Physics*, 80(11):1–15, 2009.

[3] V. M. Acosta, E. Bauch, M. P. Ledbetter, A. Waxman, L. S. Bouchard, and D. Budker. Temperature dependence of the nitrogen-vacancy magnetic resonance in diamond. *Physical Review Letters*, 104(7):1–4, 2010.

[4] B. Alberts, D. Bray, J. Lewis, M. Raff, K. Roberts, and J.D. Watson. *Molecular Biology of the Cell*. Garland, 4th edition, 2002.

[5] Mikael P. Backlund, Pauli Kehayias, and Ronald L. Walsworth. Diamond-based magnetic imaging with fourier optical processing. *Phys. Rev. Appl.*, 8:054003, Nov 2017.

[6] Gopalakrishnan Balasubramanian, Philipp Neumann, Daniel Twitchen, Matthew Markham, Roman Kolesov, Norikazu Mizuochi, Junichi Isoya, Jocelyn Achard, Johannes Beck, Julia Tissler, Vincent Jacques, Philip R. Hemmer, Fedor Jelezko, and Jörg Wrachtrup. Ultralong spin coherence time in isotopically engineered diamond. *Nature Materials*, 8(5):383–387, 2009.

[7] J. F. Barry, M. J. Turner, J. M. Schloss, D. R. Glenn, Y. Song, M. D. Lukin, H. Park, and R. L.

Walsworth. Optical magnetic detection of single-neuron action potentials using quantum defects in diamond. *PNAS*, 113(49):14133–14138, 2016.

[8] John F Barry, Jennifer M Schloss, Erik Bauch, Matthew J Turner, Connor A Hart, Linh M Pham, and Ronald L Walsworth. Sensitivity optimization for NV-diamond magnetometry. *Rev. Mod. Phys.*, 92(1):015004, March 2020.

[9] Erik Bauch, Connor A. Hart, Jennifer M. Schloss, Matthew J. Turner, John F. Barry, Pauli Kehayias, Swati Singh, and Ronald L. Walsworth. Ultralong Dephasing Times in Solid-State Spin Ensembles via Quantum Control. *Physical Review X*, 8(3):31025, 2018.

[10] S.D. Billings, C. Pasion, S. Walker, and L. Beran. Magnetic models of unexploded ordnance. *IEEE Transactions on Geoscience and Remote Sensing*, 44(8):2115–2124, 2006.

[11] D. A. Broadway, B. C. Johnson, M. S.J. Barson, S. E. Lillie, N. Dontschuk, D. J. McCloskey, A. Tsai, T. Teraji, D. A. Simpson, A. Stacey, J. C. McCallum, J. E. Bradby, M. W. Doherty, L. C.L. Hollenberg, and J. P. Tetienne. Microscopic Imaging of the Stress Tensor in Diamond Using in Situ Quantum Sensors. *Nano Letters*, 19(7):4543–4550, 2019.

[12] Zev Bryant, Michael D Stone, Jeff Gore, Steven B Smith, Nicholas R Cozzarelli, and Carlos Bustamante. Structural transitions and elasticity from torque measurements on DNA. *Nature*, 424(6946):338–41, Jul 2003.

[13] C Bustamante, J F Marko, E D Siggia, and S Smith. Entropic elasticity of lambda-phage DNA. *Science*, 265(5178):1599–600, Sep 1994.

[14] Timothy E Cloutier and Jonathan Widom. Spontaneous sharp bending of double-stranded DNA. *Mol Cell*, 14(3):355–62, May 2004.

[15] Christian A. Combs and Hari Shroff. Fluorescence microscopy: A concise guide to current imaging methods. *Current Protocols in Neuroscience*, 79(1), April 2017.

[16] D M Crothers, J Drak, J D Kahn, and S D Levene. DNA bending, flexibility, and helical repeat by cyclization kinetics. *Methods Enzymol*, 212:3–29, 1992.

[17] Gijs De Lange, Toeno Van Der Sar, MacHiel Blok, Zhi Hui Wang, Viatcheslav Dobrovitski, and Ronald Hanson. Controlling the quantum dynamics of a mesoscopic spin bath in diamond. *Scientific Reports*, 2:1–5, 2012.

[18] Ken A Dill, S Banu Ozkan, M Scott Shell, and Thomas R Weikl. The protein folding problem. *Annu Rev Biophys*, 37:289–316, 2008.

[19] M. W. Doherty, F. Dolde, H. Fedder, F. Jelezko, J. Wrachtrup, N. B. Manson, and L. C.L. Hollenberg. Theory of the ground-state spin of the NV - center in diamond. *Physical Review B - Condensed Matter and Materials Physics*, 85(20):1–21, 2012.

[20] F. Dolde, H. Fedder, M. W. Doherty, T. Nöbauer, F. Rempp, G. Balasubramanian, T. Wolf, F. Reinhard, L. C.L. Hollenberg, F. Jelezko, and J. Wrachtrup. Electric-field sensing using single diamond spins. *Nature Physics*, 7(6):459–463, 2011.

[21] A. Dréau, M. Lesik, L. Rondin, P. Spinicelli, O. Arcizet, J. F. Roch, and V. Jacques. Avoiding power broadening in optically detected magnetic resonance of single NV defects for enhanced dc magnetic field sensitivity. *Physical Review B - Condensed Matter and Materials Physics*, 84(19):1–8, 2011.

[22] Aleksander V Drozdetski, Abhishek Mukhopadhyay, and Alexey V Onufriev. Strongly bent Double-Stranded DNA: Reconciling theory and experiment. *Frontiers in Physics*, 7, 2019.

[23] Quan Du, Chaim Smith, Nahum Shiffeldrim, Maria Vologodskaia, and Alexander Vologodskii. Cyclization of short DNA fragments and bending fluctuations of the double helix. *Proc Natl Acad Sci U S A*, 102(15):5397–402, Apr 2005.

[24] Tim R. Eichhorn, Claire A. Mclellan, and Ania C. Bleszynski Jayich. Optimizing the formation of depth-confined nitrogen vacancy center spin ensembles in diamond for quantum sensing. *Physical Review Materials*, 3(11):1–8, 2019.

[25] Alex Evilevitch, Laurence Lavelle, Charles M Knobler, Eric Raspaud, and William M Gelbart. Osmotic pressure inhibition of DNA ejection from phage. *Proc Natl Acad Sci U S A*, 100(16):9292–5, Aug 2003.

[26] Kejie Fang, Victor M Acosta, Charles Santori, Zhihong Huang, Kohei M Itoh, Hideyuki Watanabe, Shinichi Shikata, and Raymond G Beausoleil. High-Sensitivity Magnetometry Based on Quantum Beats in Diamond Nitrogen-Vacancy Centers. *Phys. Rev. Lett.*, 130802(March):1–5, 2013.

[27] Ilja Fescenko, Abdelghani Laraoui, Janis Smits, Nazanin Mosavian, Pauli Kehayias, Jong Seto, Lykourgos Bougas, Andrey Jarmola, and Victor M. Acosta. Diamond Magnetic Microscopy of Malarial Hemozoin Nanocrystals. *Physical Review Applied*, 11(3):1, 2019.

[28] Richard Phillips Feynman and Albert Roach Hibbs. *Quantum mechanics and path integrals*. International series in pure and applied physics. McGraw-Hill, New York, NY, 1965.

[29] L Finzi and J Gelles. Measurement of lactose repressor-mediated loop formation and breakdown in single DNA molecules. *Science*, 267(5196):378–80, Jan 1995.

[30] L Finzi and J Gelles. Measurement of lactose repressor-mediated loop formation and breakdown in single DNA molecules. *Science*, 267(5196):378–380, January 1995.

[31] Laura Finzi and Jeff Gelles. Measurement of lactose repressor-mediated loop formation and breakdown in single DNA molecules. *Science*, 267(5196):378–380, 1995.

[32] Adam Gali. Ab initio theory of the nitrogen-vacancy center in diamond. *Nanophotonics*, 8:1–34, 2019.

[33] Hernan G Garcia, Paul Grayson, Lin Han, Mandar Inamdar, Jané Kondev, Philip C Nelson, Rob Phillips, Jonathan Widom, and Paul A Wiggins. Biological consequences of tightly bent DNA: the other life of a macromolecular celebrity. *Biopolymers*, 85(2):115–30, Feb 2007.

[34] Stephanie Geggier and Alexander Vologodskii. Sequence dependence of DNA bending rigidity. *Proc. Natl. Acad. Sci. U. S. A.*, 107(35):15421–15426, August 2010.

[35] Michael Gould, Russell J. Barbour, Nicole Thomas, Hamed Arami, Kannan M. Krishnan, and Kai Mei C Fu. Room-temperature detection of a single 19nm super-paramagnetic nanoparticle with an imaging magnetometer. *Applied Physics Letters*, 105(7), 2014.

[36] Jens H. Gundlach and Stephen M. Merkowitz. Measurement of Newton's constant using a torsion balance with angular acceleration feedback. *Phys. Rev. Lett.*, 85:2869–2872, Oct 2000.

[37] P J Hagerman and V A Ramadevi. Application of the method of phage T4 DNA ligase-catalyzed ring-closure to the study of DNA structure. i. computational analysis. *J Mol Biol*, 212(2):351–62, Mar 1990.

[38] Bjørn-Ivar Haukanes and Catrine Kvam. Application of magnetic beads in bioassays. *Nature Biotechnology*, 11(1):60–63, January 1993.

[39] Sungkun Hong, Michael S. Grinolds, Linh M. Pham, David Le Sage, Lan Luan, Ronald L. Walsworth, and Amir Yacoby. Nanoscale magnetometry with NV centers in diamond. *MRS Bulletin*, 38(2):155–161, 2013.

[40] Zeeshawn Kazi, Isaac M. Shelby, Hideyuki Watanabe, Kohei M. Itoh, Vaithiyalingam Shutthanandan, Paul A. Wiggins, and Kai-Mei C. Fu. Wide-field dynamic magnetic microscopy using double-double quantum driving of a diamond defect ensemble. *Phys. Rev. Applied*, 15:054032, May 2021.

[41] Zeeshawn Kazi, Isaac M Shelby, Hideyuki Watanabe, Kohei M Itoh, Vaithiyalingam Shutthanandan, Paul A Wiggins, and Kai-Mei C Fu. Wide-Field dynamic magnetic microscopy using Double-Double quantum driving of a diamond defect ensemble. *Phys. Rev. Appl.*, 15(5):054032, May 2021.

[42] Zeeshawn Kazi, Isaac M. Shelby, Hideyuki Watanabe, Kohei M. Itoh, Vaithiyalingam Shutthanandan, Paul A. Wiggins, and Kai-Mei C. Fu. Wide-field dynamic magnetic microscopy using double-double quantum driving of a diamond defect ensemble - supplemental material. *See Supplemental Material for further NV ensemble and experimental set up details, derivation of DDQ signal, conditions for applicability of the DDQ technique, dynamic magnetic imaging videos and model information.*, 2021.

[43] P. Kehayias, M. J. Turner, R. Trubko, J. M. Schloss, C. A. Hart, M. Wesson, D. R. Glenn, and R. L. Walsworth. Imaging crystal stress in diamond using ensembles of nitrogen-vacancy centers. *Physical Review B*, 100(17):1–8, 2019.

[44] Ed E. Kleinsasser, Matthew M. Stanfield, Jannel K.Q. Banks, Zhouyang Zhu, Wen Di Li, Victor M. Acosta, Hideyuki Watanabe, Kohei M. Itoh, and Kai Mei C. Fu. High density nitrogen-vacancy sensing surface created via He+ion implantation of12C diamond. *Applied Physics Letters*, 108(20), 2016.

[45] Daniel T Kovari, Yan Yan, Laura Finzi, and David Dunlap. Topology and Transcription Factor Interactions. *Methods Mol Biol.*, 1665:317–340, 2018.

[46] Jonathan C. Lansey. (2023) beautiful and distinguishable line colors + colormap (https://www.mathworks.com/matlabcentral/fileexchange/42673-beautiful-and-distinguishable-line-colors-colormap), matlab central file exchange. Retrieved August 18, 2023.

[47] Paul Lebel, Aakash Basu, Florian C Oberstrass, Elsa M Tretter, and Zev Bryant. Gold rotor bead tracking for high-speed measurements of DNA twist, torque and extension. *Nature Methods*, 11(4):456–462, February 2014.

[48] Edlyn V. Levine, Matthew J. Turner, Pauli Kehayias, Connor A. Hart, Nicholas Langellier, Raisa Trubko, David R. Glenn, Roger R. Fu, and Ronald L. Walsworth. Principles and techniques of the quantum diamond microscope. *Nanophotonics*, 2019.

[49] Edlyn V Levine, Matthew J Turner, Pauli Kehayias, Connor A Hart, Nicholas Langellier, Raisa Trubko, David R Glenn, Roger R Fu, and Ronald L Walsworth. Principles and techniques of the quantum diamond microscope. *Nanophotonics*, 8(11):1945–1973, November 2019.

[50] M Lewis, G Chang, N C Horton, M A Kercher, H C Pace, M A Schumacher, R G Brennan, and P Lu. Crystal structure of the lactose operon repressor and its complexes with DNA and inducer. *Science*, 271(5253):1247–54, Mar 1996.

[51] Bing Li, Yang Cao, Eric Westhof, and Zhichao Miao. Advances in RNA 3D structure modeling using experimental data. *Front Genet*, 11:574485, 2020.

[52] Eduardo A Lima and Benjamin P Weiss. Obtaining vector magnetic field maps from single-component measurements of geological samples. *J. Geophys. Res. [Solid Earth]*, 114(B6), 2009.

[53] H. J. Mamin, M. H. Sherwood, M. Kim, C. T. Rettner, K. Ohno, D. D. Awschalom, and D. Rugar. Multipulse double-quantum magnetometry with near-surface nitrogen-vacancy centers. *Physical Review Letters*, 113(3):1–5, 2014.

[54] J F Marko and E D Siggia. Fluctuations and supercoiling of DNA. *Science*, 265(5171):506–8, Jul 1994.

[55] Alexander J Mastroianni, David A Sivak, Phillip L Geissler, and A Paul Alivisatos. Probing the conformational distributions of subpersistence length DNA. *Biophys J*, 97(5):1408–17, Sep 2009.

[56] Alexey K Mazur and Mounir Maaloum. Atomic force microscopy study of DNA flexibility on short length scales: smooth bending versus kinking. *Nucleic Acids Res*, 42(22):14006–12, Dec 2014.

[57] Alexey K Mazur and Mounir Maaloum. DNA flexibility on short length scales probed by atomic force microscopy. *Phys Rev Lett*, 112(6):068104, Feb 2014.

[58] Julia M. McCoey, Robert W. de Gille, Babak Nasr, Jean Philippe Tetienne, Liam T. Hall, David A. Simpson, and Lloyd C.L. Hollenberg. Rapid, High-Resolution Magnetic Microscopy of Single Magnetic Microbeads. *NanoMicroSmall*, 15(18):1–9, 2019.

[59] H Merlitz, K Rippe, K V Klenin, and J Langowski. Looping dynamics of linear dna molecules and the effect of DNA curvature: a study by brownian dynamics simulation. *Biophys J*, 74(2 Pt 1):773–9, Feb 1998.

[60] T. Mittiga, S. Hsieh, C. Zu, B. Kobrin, F. Machado, P. Bhattacharyya, N. Z. Rui, A. Jarmola, S. Choi, D. Budker, and N. Y. Yao. Imaging the Local Charge Environment of Nitrogen-Vacancy Centers in Diamond. *Physical Review Letters*, 121(24):1–6, 2018.

[61] Alexandre V Morozov, Karissa Fortney, Daria A Gaykalova, Vasily M Studitsky, Jonathan Widom, and Eric D Siggia. Using DNA mechanics to predict in vitro nucleosome positions and formation energies. *Nucleic Acids Res*, 37(14):4707–22, Aug 2009.

[62] B. A. Myers, A. Ariyaratne, and A. C.Bleszynski Jayich. Double-Quantum Spin-Relaxation Limits to Coherence of Near-Surface Nitrogen-Vacancy Centers. *Physical Review Letters*, 118(19):1–7, 2017.

[63] S Oehler, M Amouyal, P Kolkhof, B von Wilcken-Bergmann, and B Müller-Hill. Quality and position of the three *lac* operators of *E. coli* define efficiency of repression. *EMBO J*, 13(14):3348–55, Jul 1994.

[64] Kenichi Ohno, F. Joseph Heremans, Charles F. De Las Casas, Bryan A. Myers, Benjamín J. Alemán, Ania C. Bleszynski Jayich, and David D. Awschalom. Three-dimensional localization of spins in diamond using 12C implantation. *Applied Physics Letters*, 105(5), 2014.

[65] W K Olson, A A Gorin, X J Lu, L M Hock, and V B Zhurkin. DNA sequence-dependent deformability deduced from protein-DNA crystal complexes. *Proc Natl Acad Sci U S A*, 95(19):11163–8, Sep 1998.

[66] Christian Osterkamp, Martin Mangold, Johannes Lang, Priyadharshini Balasubramanian, Tokuyuki Teraji, Boris Naydenov, and Fedor Jelezko. Engineering preferentially-aligned nitrogen-vacancy centre ensembles in CVD grown diamond. *Scientific Reports*, 9(1):1–7, 2019.

[67] L. M. Pham, D. Le Sage, P. L. Stanwix, T. K. Yeung, D. Glenn, A. Trifonov, P. Cappellaro, P. R. Hemmer, M. D. Lukin, H. Park, A. Yacoby, and R. L. Walsworth. Magnetic field imaging with nitrogen-vacancy ensembles. *New Journal of Physics*, 13, 2011.

[68] Rob Phillips, Jane Kondev, and Julie Theriot. *Physical Biology of the Cell*. Garland Science, Taylor & Francis Group, New York, November 2008.

[69] Prashant K Purohit, Jané Kondev, and Rob Phillips. Mechanics of DNA packaging in viruses. *Proc Natl Acad Sci U S A*, 100(6):3173–8, Mar 2003.

[70] Timothy J Richmond and Curt A Davey. The structure of DNA in the nucleosome core. *Nature*, 423(6936):145–50, May 2003.

[71] C Rivetti, M Guthold, and C Bustamante. Scanning force microscopy of DNA deposited onto mica: equilibration versus kinetic trapping studied by statistical polymer chain analysis. *J Mol Biol*, 264(5):919–32, Dec 1996.

[72] Kento Sasaki, Yasuaki Monnai, Soya Saijo, Ryushiro Fujita, Hideyuki Watanabe, Junko Ishi-Hayase, Kohei M. Itoh, and Eisuke Abe. Broadband, large-area microwave antenna for optically detected magnetic resonance of nitrogen-vacancy centers in diamond. *Review of Scientific Instruments*, 87(5), 2016.

[73] Romana Schirhagl, Kevin Chang, Michael Loretz, and Christian L. Degen. Nitrogen-Vacancy Centers in Diamond: Nanoscale Sensors for Physics and Biology. *Annual Review of Physical Chemistry*, 65(1):83–105, 2014.

[74] Yechezkel Schlussel, Till Lenz, Dominik Rohner, Yaniv Bar-Haim, Lykourgos Bougas, David Groswasser, Michael Kieschnick, Evgeny Rozenberg, Lucas Thiel, Amir Waxman, Jan Meijer, Patrick Maletinsky, Dmitry Budker, and Ron Folman. Wide-Field Imaging of Superconductor Vortices with Electron Spins in Diamond. *Physical Review Applied*, 10(3):1, 2018.

[75] Eran Segal, Yvonne Fondufe-Mittendorf, Lingyi Chen, AnnChristine Thåström, Yair Field, Irene K Moore, Ji-Ping Z Wang, and Jonathan Widom. A genomic code for nucleosome positioning. *Nature*, 442(7104):772–8, Aug 2006.

[76] J Shimada and H Yamakawa. Ring-closure probabilities for twisted wormlike chains. application to DNA. *Macromolecules*, 17:689–698, 1984.

[77] D Shore, J Langowski, and R L Baldwin. DNA flexibility studied by covalent closure of short fragments into circles. *Proc Natl Acad Sci U S A*, 78(8):4833–7, Aug 1981.

[78] B Simpson, C Tupper, and N M Al Aboud. Genetics, DNA packaging. https://europepmc.org/article/nbk/nbk534207. Accessed: 2023-6-22.

[79] D E Smith, S J Tans, S B Smith, S Grimes, D L Anderson, and C Bustamante. The bacteriophage straight phi29 portal motor can package DNA against a large internal force. *Nature*, 413(6857):748–52, Oct 2001.

[80] S. Steinert, F. Ziem, L. T. Hall, A. Zappe, M. Schweikert, N. Götz, A. Aird, G. Balasubramanian, L. Hollenberg, and J. Wrachtrup. Magnetic spin imaging under ambient conditions with sub-cellular resolution. *Nature Communications*, 4, 2013.

[81] Kevin Struhl and Eran Segal. Determinants of nucleosome positioning. *Nat Struct Mol Biol*, 20(3):267–73, Mar 2013.

[82] J. P. Tetienne, R. W. De Gille, D. A. Broadway, T. Teraji, S. E. Lillie, J. M. McCoey, N. Dontschuk, L. T. Hall, A. Stacey, D. A. Simpson, and L. C.L. Hollenberg. Spin properties of dense near-surface ensembles of nitrogen-vacancy centers in diamond. *Physical Review B*, 97(8):1–11, 2018.

[83] Jean Philippe Tetienne, Nikolai Dontschuk, David A. Broadway, Alastair Stacey, David A. Simpson, and Lloyd C.L. Hollenberg. Quantum imaging of current flow in graphene. *Science Advances*, 3(4), 2017.

[84] A Thåström, P T Lowary, H R Widlund, H Cao, M Kubista, and J Widom. Sequence motifs and free energies of selected natural and non-natural nucleosome positioning DNA sequences. *J Mol Biol*, 288(2):213–29, Apr 1999.

[85] A A Travers and J M T Thompson. An introduction to the mechanics of DNA. *Philos. Trans. A Math. Phys. Eng. Sci.*, 362(1820):1265–1279, July 2004.

[86] Reza Vafabakhsh and Taekjip Ha. Extreme bendability of DNA less than 100 base pairs long revealed by single-molecule cyclization. *Science*, 337(6098):1097–101, Aug 2012.

[87] Reza Vafabakhsh and Taekjip Ha. Extreme bendability of DNA less than 100 base pairs long revealed by single-molecule cyclization. *Science*, 337(6098):1097–1101, August 2012.

[88] M Y Vologodskaia and A V Vologodskii. Effect of magnesium on cruciform extrusion in supercoiled DNA. *J Mol Biol*, 289(4):851–9, Jun 1999.

[89] Maria Vologodskaia and Alexander Vologodskii. Contribution of the intrinsic curvature to measured DNA persistence length. *J Mol Biol*, 317(2):205–13, Mar 2002.

[90] Alexander Vologodskii and Maxim D Frank-Kamenetskii. Strong bending of the DNA double helix. *Nucleic Acids Res*, 41(14):6785–92, Aug 2013.

[91] Paul A Wiggins and Philip C Nelson. Generalized theory of semiflexible polymers. *Phys Rev E Stat Nonlin Soft Matter Phys*, 73(3 Pt 1):031906, Mar 2006.

[92] Paul A Wiggins and Philip C Nelson. Generalized theory of semiflexible polymers. *Phys. Rev. E Stat. Nonlin. Soft Matter Phys.*, 73(3 Pt 1):031906, March 2006.

[93] Paul A Wiggins, Thijn van der Heijden, Fernando Moreno-Herrero, Andrew Spakowitz, Rob Phillips, Jonathan Widom, Cees Dekker, and Philip C Nelson. High flexibility of DNA on short length scales probed by atomic force microscopy. *Nat Nanotechnol*, 1(2):137–41, Nov 2006.

[94] E Winfree, F Liu, L A Wenzler, and N C Seeman. Design and self-assembly of two-dimensional DNA crystals. *Nature*, 394(6693):539–44, Aug 1998.

[95] Adam M. Wojciechowski, Mürsel Karadas, Alexander Huck, Christian Osterkamp, Steffen Jankuhn, Jan Meijer, Fedor Jelezko, and Ulrik L. Andersen. Camera-limits for wide-field magnetic resonance imaging with a nitrogen-vacancy spin sensor. *Review of Scientific Instruments*, 89(3), 2018.

[96] Yongli Zhang and Donald M Crothers. Statistical mechanics of sequence-dependent circular DNA and its application for DNA cyclization. *Biophys J*, 84(1):136–53, Jan 2003.

[97] Yongli Zhang, Abbye E McEwen, Donald M Crothers, and Stephen D Levene. Statistical-mechanical theory of DNA looping. *Biophys J*, 90(6):1903–12, Mar 2006.

[98] Yongli Zhang, Zhiqun Xi, Rashmi S Hegde, Zippora Shakked, and Donald M Crothers. Predicting indirect readout effects in protein-DNA interactions. *Proc Natl Acad Sci U S A*, 101(22):8337–41, Jun 2004.

[99] Jianping Zheng, Jens J Birktoft, Yi Chen, Tong Wang, Ruojie Sha, Pamela E Constantinou, Stephan L Ginell, Chengde Mao, and Nadrian C Seeman. From molecular to macroscopic via the rational design of a self-assembled 3D DNA crystal. *Nature*, 461(7260):74–7, Sep 2009.

Appendix A

Biological Protocols

A.1 PCR

Polymerase Chain Reaction is a powerful method for generating DNA in the lab.

The core of this approach relies on a polymerase that is not denatured at the melting tempreature of DNA. The core loop of PCR is: heat to melt dsDNA to ssDNA, cool to allow primers to anneal to ssDNA, heat to allow Taq polymerase to convert ssDNA to dsDNA, repeat. The primers step allows selection of a specific region of the initial template DNA due to the polymerase needing to start from a region of dsDNA and go 5' to 3'.

Starting with a template DNA, the desired subsection of the template is selected by choosing two "primers." The primer is typically a 20 basepair section of the DNA, with roughly 50% GC content and a GC clamp at the 3' end of the primer. Adhering to these qualities helps ensure that the primer adheres appropriately (and specifically) to the single stranded DNA. It is additionally important to check the ΔG for the primer to interact with itself or another identical primer is more positive than around -9 kcal/mol. This number is not a hard limit, but as it becomes more negative, the PCR reaction generates less of the target product.

It is worth noting that this reaction does not purely generate the target dsDNA. There are a variety of structures that form as well due to the original template DNA, but their quantity grows linearly (as opposed to the exponential growth of the target dsDNA).

Two ways to introduce functionalization to the DNA are: use oligos with specific moities attached (offered by many suppliers of lab synthesized DNA) or use modified nucleotides that have the desired moiety attached.

The following protocol was used for generation of all DNA constructs. Specific primer sequences and template DNA will be listed afterwards.

DNA oligos were ordered from Integrated DNA Technologies (IDT). DNA template pUC18 was provided by Sarah Mangiameli. Taq polymerase, ThermoPol Buffer, and dNTPs purhcased from New England Biolabs.

Quantities listed are for a 100 uL total volume reaction.

dNTPs : 2 uL (200 uM final concentration)

buffer (10x stock): 10 uL

DNA template: 1 uL (<1 ug)

Forward Primer: volume to have 0.2 uM final concentration

Reverse Primer: volume to have 0.2 uM final concentration

Taq Polymerase: 1 uL

Water (sterile and nuclease free): up to 100 uL

1. Get tube rack with ice tray to keep components chilled until reaction is started. Not entirely necessary for a PCR reaction given the high temperature required for the enzyme to be active, but good practice to increase longevity of components.

2. Thaw frozen components: dNTPs , buffer

3. Add predetermined amount of water to epi tube. Add DNA template, forward primer, and reverse primer.

4. Add dNTPs and buffer. If including modified dUTPs to introduce moieties along the length of a piece of DNA, add here as well. We added enough dUTPs to have the ratio of T:U in the mixture be 3:1. This spaces the dUTPs 1 every 3 T's on average. For torsionally constrained tethers, we generated DNA "feet" with biotin (to attach to the streptavidin coated beads) and other "feet" with digoxigenin (to attach to the anti-digoxigenin coated coverslip or diamond surface).

5. Get Taq from freezer, add. Place epi tube with all components firmly in ice. Return all components to fridge/freezer.

6. Gently pipette contents of epi tube up and down to mix, then transfer into tube for thermocycler (usually 50 uL per thermocycler tube).

7. Place tubes in thermocycler, follow instructions on proper placement and sealing on inside of cover.

8. Run PCR program on thermocycler. An example PCR program is listed below (temperatures in Celsius):

a) 95 for 5 minutes (initial melting)

b) 55 for 1 minute (annealing primers)

c) 72 for 1 minute/kbp of final product, no less than 1 minute (polymerase action)

d) if c) has been reached less than 30 times, 95 for 1 minute and return to b), else continue to e)

e) 72 for 5 minutes (supposed to give polymerase chance to fix any incomplete areas)

f) some protocols recommend putting the thermocycler to 4 Celsius afterwards, we have found this unnecessary, even if unable to retrieve DNA immediately after cycles complete.

The temperature in b) is commonly varied depending on the melting temperature of the primers being used.

9. Get tubes from thermocycler, and run DNA cleaning protocol discussed in Section A.4

10. Use a NanoDrop or similar device to determine the concentration (ng/uL) of the DNA product. Then run a gel to verify length. When generating these constructs with idealized primers, incorrect structures or secondary products are rare, but can still be worth checking for.

A.1.1 Relevant DNA sequences

This section lists templates for PCR reactions and primers used in generating DNA complexes used in this thesis.

Unconstrained DNA tethers

Much simpler than constrained tethers, we simply had moieties attached to the end of the DNA olgios functions as primers for the PCR reaction. The construct is finished after one PCR reaction.

Template: pUC18 (selected location: 2524-761)

forwards primer: GGT TAT TGT CTC ATG AGC GG (with 5' digoxigenin modification)

reverse primer: CCT TTG AGT GAG CTG ATA CC (with 3' biotin modification)

Constrained DNA tethers

Requiring 3 separate sections to be ligated together later, there are 3 required PCR reaction to construct these. One for each of the feet, and one for the DNA construct to be measured.

Foot 1:

Template: pUC18

forwards primer: ATG ATC CCC CAT GTT GTG CA

reverse primer (with ApaI cut site): ATC GAT GGG CCC CCA GAA ACG CTG GTG AAA GT

Foot 2:

Template: pUC18

forwards primer (with SacII cut site): ATC GAT CCG CGG CGG TTA TCC ACA GAA TCA GG

reverse primer: GGT TGG ACT CAA GAC GAT AG

Construct to measure (150, 300, 600 BP):

All use the same forwards primer, and different reverse primers

Template: pUC18

forwards primer (with ApaI cut site): ATC GAT GGG CCC GGT TAT TGT CTC ATG AGC GG

600 BP reverse primer (with SacII cut site): ATC GAT CCG CGG CAC AGG AAA CAG CTA TGA CC

300 BP reverse primer (with SacII cut site): ATC GAT CCG CGG CTG ATG CCG CAT AGT TAA GC

150 BP reverse primer (with SacII cut site): ATC GAT CCG CGG GCC TCG TGA TAC GCC TAT TT

A.2 DNA cutting

An important method of manipulating strands of DNA is cutting them. One such method involves using restriction enzymes. Restriction enzymes can be purchased from a variety of places, and target specific sequences. The most commonly used enzymes target 6 base-pair sequences that are often symmetric (i.e.

the 5'-3' on both strands reads identically). For the sake of this thesis, restriction enzyme cutting was used as an intermediate step for generating the torsionally-bound constrained DNA molecules.

Using the methods described in Section A.1, you begin by generating 3 strands: 1 400 bp DNA molecule "foot" with digoxigenin (dig) introduced by adding dUTPs with dig (PART REF) to the PCR reaction, 1 400 bp DNA molecule "foot" with biotin introduced by adding dUTPs with biotin (PART REF) to the PCR reaction, the DNA sequence to be studied. As discussed in Section A.3, to generate the full construct, these three have to be ligated together. To improve the chances of ligation in the desired format, one can include a target sequence for restriction enzyme digesting on the ends of the sub-units to be attached. This is done by modifying the original 20 basepairs of homology in a primer to include an additional 12 basepairs: 6 to match the target sequence, and 6 so the target sequence is not on the end of the molecule (this reduces cutting efficiency). By including the same restriction enzyme target on the ends of two pieces of DNA that will be ligated, it allows for "sticky" end ligation (as opposed to "blunt" end). Due to the symmetric nature of the restriction target, the overhangs are complementary, and this improves the likelihood of successful ligation of those two molecules.

In the context of this thesis, further care went into the selection of restriction enzymes. Because the selected approach for introducing moieties to the "feet" of the tether was dUTPs (which subsitutioanlly replace T's in the final molecule), restriction enzyme target sequences without T's (and consequently without A's) were chosen. These are ApaI and SacII purchased from New England Biolabs (NEB).

Restrictions are relatively straight forward, but are an important step in the construction of these DNA tethers.

Components:

DNA to cut: 1 ug

restriction enzyme: 1 uL

10x buffer: 5 uL

sterile (nuclease free) water: up to 50 uL

1. Prepare tube rack with ice tray.

2. Retrieve DNA and buffer. Thaw buffer if applicable.

3. Add DNA and buffer to water in epi tube. Store in iced tube rack. Return components to storage. Retrieve restriction enzyme.

4. Add 1 uL restriction enzyme. Put back on ice. Return enzyme to storage.

5. Gently pipette mixture up and down. You can transfer to a thermocycler tube and run the digestion in the thermocycler, or just use a heatblock. Different enzymes may have different suggested temperatures and durations for the digestion, but they are typically 37 Celsius for 1 hour.

6. If you are able to get the sample and run a DNA cleaning protocol when the hour is up, do so. If you are unable to conduct the cleaning until later, you may have the thermocycler go up to the listed heat inactivation temperature for the recommended time (usually 65 Celsius for 20 minutes). Still clean the DNA when you retrieve it.

A.3 DNA tether construction

The least consistent step in the construction process of the torsionally constrained tethers is the ligation. In sticky end ligation, the components of the final product are mixed, and ligase stitches the backbone of the DNA together once the complementary regions have annealed. It is important to run the appropriate restriction enzyme digests on the corresponding DNA fragments before running the ligation. The ratio of more feet to fragments reduces the likelihood of multiple of the DNA fragment to study being ligated together. Buffer and ligase purchased from New England Biolabs, protocol taken modeled off their provided protocol:
Components:
T4 Dna ligase buffer (10x) (NEB): 2 uL
DNA Foot 1 (0.06 picomoles)
DNA Foot 2 (0.06 picomoles)
DNA fragment to study (0.02 picomoles)
T4 DNA ligase
nuclease-free water: to 20 uL

1. Combine all ingredients. Incubate at room temperature for 10-15 minutes.

2. Heat inactivate: 65 Celsius for 10 minutes.

3. Clean reaction using protocol discussed in Section A.4. It was useful to run 2-5 of these 20 uL reactions in parallel and clean together to give a higher final concentration after cleaning.

A.4 DNA cleanup

After any of the DNA protocols listed above, it is important to "clean" your final product. Unused initial components, buffers oriented towards optimizing reaction yield instead of sample longevity, and enzymes should be removed from the sample. For the constructs discussed in this thesis, the restriction enzyme digestions were run immediately before the ligation, so no cleaning step was required (but the enzymes were denatured).

For DNA cleaning, we used the QIAquick PCR purification Kit, and followed the protocol for using it in conjuction with a centrifuge. Our only adjustment was we heated the final elution buffer (they refer to it as Buffer EB) to 37 Celsius in a heat block to improve extraction of the final product from the QIAquick column.